Development of Thin Film Nickel Hydroxide Electrochromic Materials using *in situ* Microfocus XAFS and XRD Techniques

By

David C C Cutler

A Master's Thesis

Submitted in Partial Fulfilment of the Requirements for the Award of

Master of Philosophy of Loughborough University.

Abstract

The use of nickel hydroxide as a colour switching material in electrochromic devices such as smart windows is yet to be fully exploited. Stabilisation of the highly electroactive α nickel hydroxide / γ nickel oxyhydroxide redox couple through co-deposition of other metal ions could lead to devices with improved performance in terms of response time and cycle lifetime. This thesis presents the current understanding of nickel hydroxide phases and their relationship to one another, various ways to form nickel hydroxide materials and the effect of doping nickel hydroxide materials with cobalt, cadmium, zinc, manganese, iron, aluminium ions. In addition, this thesis describes the basic components of an *in situ* electrochemical cell and compares *in situ* cell designs used to study electrochemically active thin films under potential control with synchrotron light sources.

The thesis follows with a description of the synthesis of various phases of nickel hydroxide via chemical precipitation to form powder and the electrochemical deposition method to deposit thin films and demonstrates the development of a novel *in situ* electrochemical flow cell, designed for *in situ* XAFS analysis of nickel hydroxide thin films under potential control.

The thesis also highlights that this is the first time a transparent conductive oxide coated polymer film is used as both a working electrode and x-ray window material for an *in situ* electrochemical cell.

Contents

Acknowledgements

I would like to take this opportunity to say thank you to Dr Caroline Kirk and Professor Fred Mosselmans for their patience, support and motivation through this project. I am also grateful for your guidance and wish the best of luck to you and your teams for the future.

I would also like to say thank you to the many friends I made along the way, both post-graduate and staff, your support during the difficult times made it possible to finish this work.

I would also like to thank the STFC for their funding and giving me the opportunity to experience the Harwell Science campus first hand, one of the UK's most advanced scientific establishments.

I would also like to say thank you to the I18 and I08 beamline staff, who made me feel very welcome and I especially want to thank Dr Steven Price for his support, patience and knowledge during my time in Oxfordshire.

I also want to say thank you to Dr Paul Shearing and the STFC Batteries group for awarding me with the STFC batteries early career award which enabled me to travel to Italy and visit the Elettra Synchrotron facility.

I would like to also say thank you to Benedetto Bozzini, Alessandra Gianoncelli, and Simone Dal Zilio for their time and making me feel welcomed during my stay in Trieste.

Finally I would like to say thank you to Professor Roger Mortimer, who I have had the pleasure of working with on several projects and who supported me during my industrial placement, I was always proud to have you as a supervisor, this work is dedicated to you.

Chapter 1

Literature Review

1.1 Introduction and background

For over a century nickel hydroxide (or hydrated nickel oxide) has been of great interest to material chemists due to its applications in energy storage devices such as rechargeable alkaline batteries[1]. More recent developments have included its use in supercapacitors[2], electrochemical sensors[3] and electrochromic devices[4].

Electrochromism is a phenomenon which causes a material to reversibly change colour with an applied electric potential. Electrochromic devices can therefore be fabricated from nickel hydroxide as it changes colour. It has also been shown that electrochemical performance of nickel hydroxide materials can be improved through the addition of other metallic elements, these elements either replace the Ni^{2+} ions in the layers, or are placed between layers within the crystal structure along with charge balance counter ions.

There have been several comprehensive reviews over the years, however this thesis concentrates on the most significant early work conducted by Bode et al[5]. The group established that both nickel (II) hydroxide and nickel (III) oxyhydroxide could exist in different forms which could be transformed into one another. After several years, a significant review was published by Oliva et al[6] in 1982, which collated the most important work prior to its publication and presented a clearer understanding of the nickel hydroxide redox couple for secondary batteries. It should also be noted that the recent literature review by Hall, Lockwood, Bock and MacDougall[7] provides a comprehensive and modern understanding of nickel hydroxide based materials and is highly recommended to any researcher working in this field.

1.2 Aims and objectives

The first aim was to investigate how changes to synthesis routes, electrochemical cycling and doping of other elements affected the crystal structure of nickel hydroxide materials.

The aims were achieved through several objectives, the first objective was to synthesise and characterise samples to be used as standards of the various nickel hydroxide phases and for comparison to phase transitions in nickel hydroxide thin films, using powder X-ray diffraction (XRD) and Fourier-transform infrared spectroscopy (FTIR).

The secondary aim was to study changes in the structure of nickel hydroxide and doped nickel hydroxide materials under an applied electric field using X-ray absorption fine structure (XAFS) and XRD techniques.

This objective was to be achieved through the development of an *in situ* electrochemical flow cell which was designed for the I18 microfocus XAFS beamline at the Diamond Light Source synchrotron facility and monitor the changes in atomic position during electrochemical cycling of nickel hydroxide thing films.

1.3 Literature review

Approximately 30 - 40% of a building's energy usage is expended on heating, cooling, lighting and ventilation.[8] "Smart window" technology based on electrochromic devices can save energy through enabling occupants to modulate the level of light transmitted through windows via an electrical pulse. Tinting windows in such a way can reduce the transmittance of heat / light energy from the sun. Thus reducing the cooling load on air conditioning units, reducing the size of the required air conditioning unit or removing the need for them entirely, whilst still maintaining a comfortable temperature with improved comforted through reduced glare.

Smart window technology relies on colour switching electrochromic materials for their function. One such material, which is yet to be fully explored is nickel hydroxide, $Ni(OH)_2$ also known as hydrated nickel oxide. Nickel hydroxide has been extensively researched as a charge storage material for over a century[9] and has led to the commercial success of secondary batteries such as nickel cadmium[1] (NiCd- no longer used due to health concerns[10]), nickel metal hydride[11] (NiMH) and less well known, nickel hydrogen[12] (NiH_2), where NiH_2 batteries are specifically used for their reliability in space applications. However, in recent years other applications of nickel hydroxide have been realised including, but not limited to; supercapacitors[2,13], photo-electrochemical thin films[14], electrochemical sensors[3] and water splitting catalysts[15].

1.4 Structure of nickel hydroxide materials

Nickel hydroxide has been extensively characterised over many years by spectroscopic, electrochemical and structural techniques. However, due to the complex nature of these materials, progress into understanding this material's structure was initially slow. Bode's early reaction scheme (figure 1.1) established that both nickel (II) hydroxide and the oxidised form nickel (III) oxyhydroxide could

exist in different polymorphs, known as α-$Ni(OH)_2$, β-$Ni(OH)_2$, γ-NiOOH and β-NiOOH.

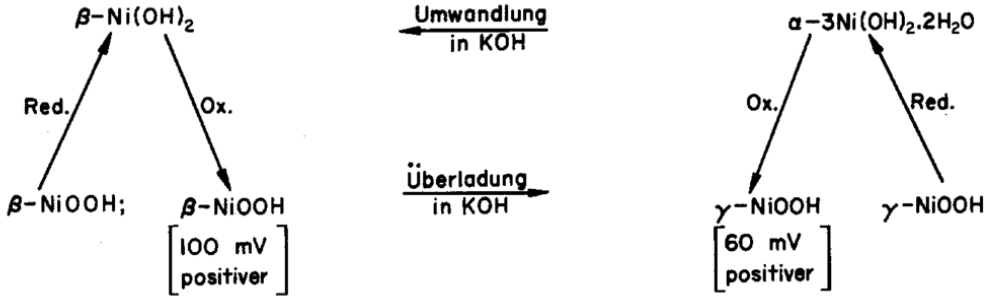

Figure 1.1 - Original Bode reaction scheme[16]

Additional reaction pathways have been realised since the original concept, including the direct transformation of γ nickel (III) oxyhydroxide to β nickel (II) hydroxide as shown below in figure 1.2.

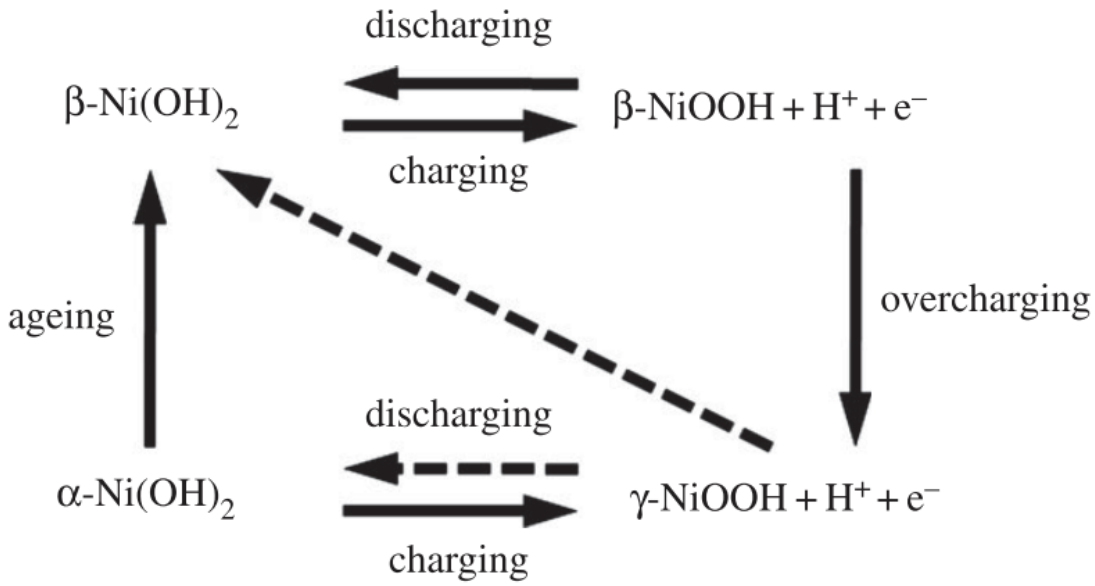

Figure 1.2 - Modern depiction of Bode reaction scheme[7]

1.4.1 Beta nickel hydroxide (β-Ni(OH)$_2$)

β-Ni(OH)$_2$ is isostructural with brucite (Mg(OH)$_2$) and consists of Ni(OH)$_6$ octahedral layers/sheets, with the octahedra sharing edges. It crystallises in the space group $P\bar{3}m1$ with lattice parameters a=3.126 Å and c=4.605 Å[6]. The structure can be described as hexagonally close packed hydroxyl ions (AB stacking) with Ni(II) cations occupying octahedral interstices on alternate plane/ layers (figure 1.3). Bonding within the layers is predominantly ionic, however bonding between layers is due to Van der Waals forces.

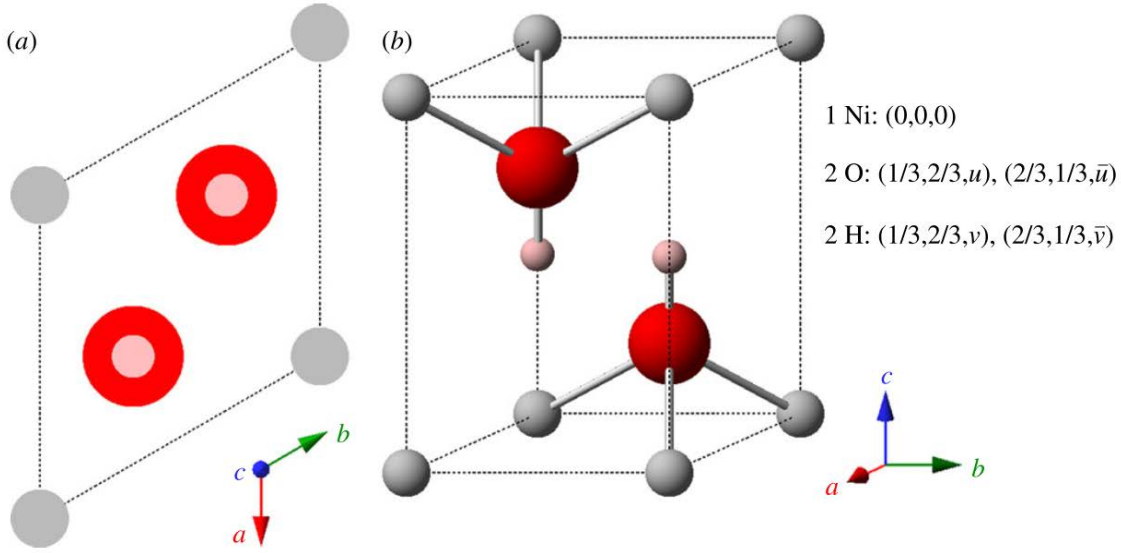

Figure 1.3 - Crystal structure of β-Ni(OH)$_2$, (a) unit cell projection (b) ball and stick model with described atomic positions of nickel (grey) oxygen (red) and hydrogen (pink) atoms.[7]

Theophrastite[17] is a naturally occurring mineral closely related to β-Ni(OH)$_2$. Theophrastite can be found on surfaces and fractures of ores of millerite (NiS) and crystallises in the trigonal space group $P\bar{3}m1$ with lattice parameters *a* = 3.131 Å and *c* = 4.608 Å. Like synthetic β-Ni(OH)$_2$, it is normally highly crystalline and shows a much smaller *c* parameter than α-Ni(OH)$_2$, as described below.[17]

β-$Ni(OH)_2$ is well characterised in the literature[7] and can be easily identified using FTIR and XRD techniques. The FTIR spectrum of β-$Ni(OH)_2$ has a characteristic narrow absorption band around 3650 cm^{-1} which is attributed to the stretching vibration of non-hydrogen bonded OH^- and so shows that no hydrogen bonding is present between the stacked layers (OH). Other bands which can be observed include: the in-plane deformation at 520 cm^{-1} (OH), the out of plane deformation at 345 cm^{-1} (OH) and the Ni-O stretching vibration at 460 cm^{-1} (NiO)[6].

1.4.2 Alpha nickel hydroxide (α-$Ni(OH)_2$)

α-$Ni(OH)_2$ has been described as a hydrated pseudopolymorph of nickel hydroxide with a randomly ordered structure. The structure is described as water or charge balancing anions intercalated in-between turbostratic brucite like $Ni(OH)_2$ layers. This poorly ordered material is hydroxyl deficient and has been formulated as $Ni(OH)_{2-x}(A^{n-})_{x/n}\cdot mH_2O$, where A^{n-} = Cl^-, NO_3^- or SO_4^{2-}, x = 0.15 – 0.20 and m = 0.66 – 0.75.[18]

As shown in figure 1.4, the FTIR spectrum of α-$Ni(OH)_2$ phase has a broad asymmetric band around 3500 cm-^{1}, in contrast to the narrow band at 3650 cm^{-1} present in the FTIR spectrum of β-$Ni(OH)_2$. The three other bands 520, 345, 460 cm^{-1} are shifted to shorter wavelengths to those observed for β-$Ni(OH)_2$ and a band at 1600 cm^{-1} becomes apparent, caused by the angular deformation of molecular water.[6]

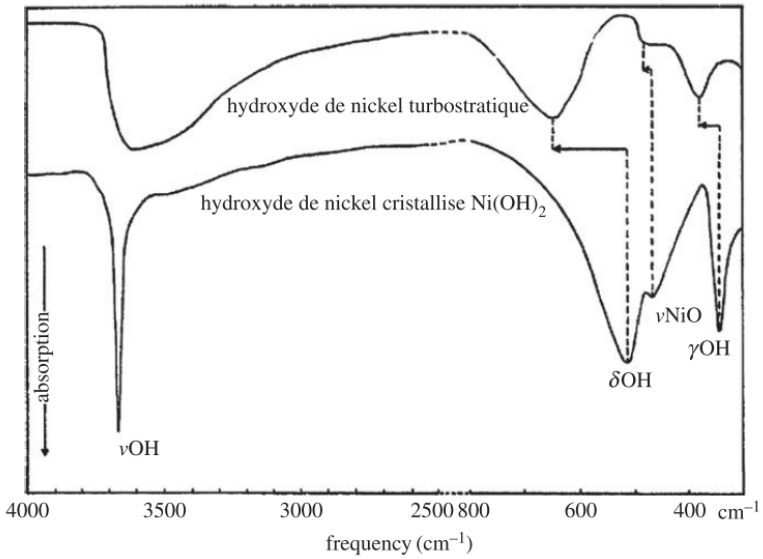

Figure 1.4 - FTIR spectrum of α-$Ni(OH)_2$ (top) and β-$Ni(OH)_2$ (bottom)[7]

It should be noted that α-$Ni(OH)_2$ does not represent a well-defined polymorph of nickel hydroxide with water intercalated between sheets (as depicted in figure 1.5). α-$Ni(OH)_2$ is used to describe nickel hydroxide materials with poor long range order, with water molecules acting as an "amorphous glue"[7] holding the crystal sheets together but with stacking faults as shown in Figure 1.6 below.

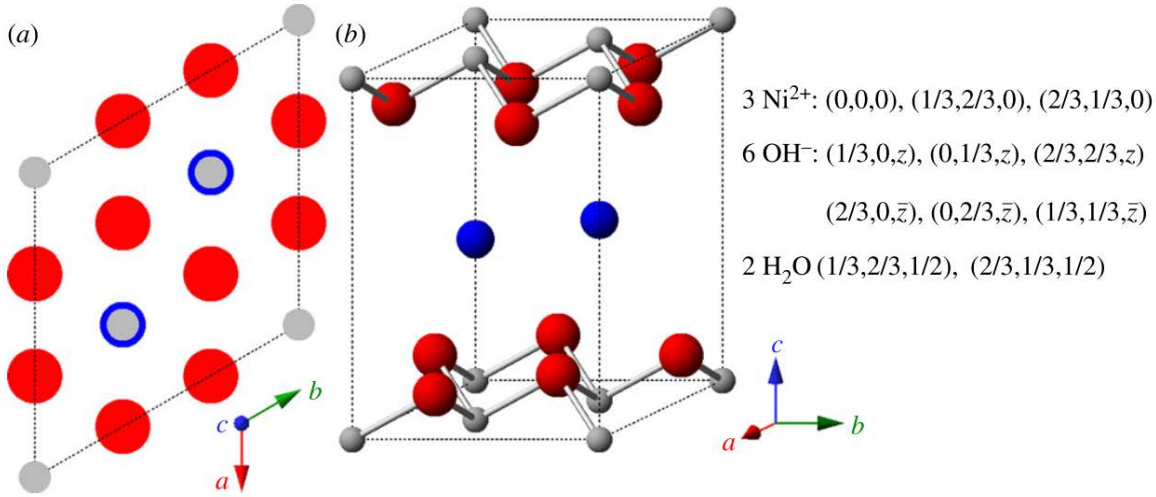

Figure 1.5 - Crystal structure of α-$Ni(OH)_2.H_2O$, nickel (grey) hydroxide ions (red) water molecules (blue) (a) unit cell projection (b) ball and stick model with atomic positions.[7]

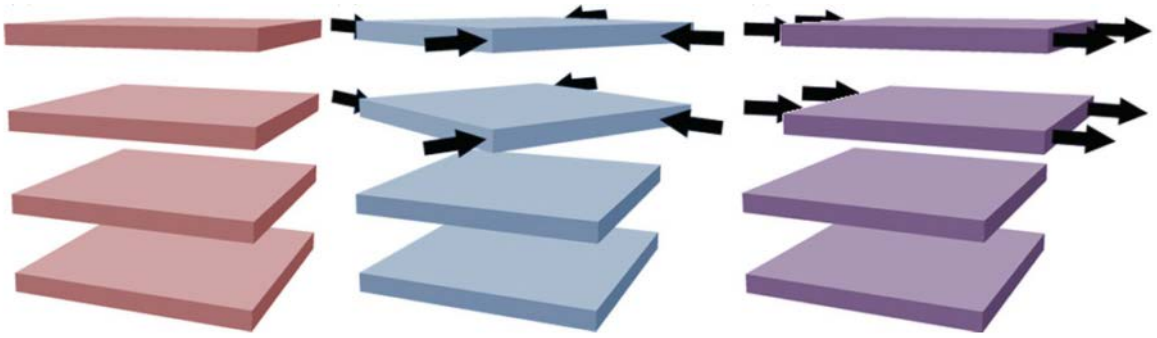

Figure 1.6 – Schematic illustrating stacking fault disorder between adjacent layers. (Red) no stacking faults and adjacent layers are aligned. (Blue) Rotation about the crystallographic *c* axis. (Purple) translation within the *ab* plane.[7]

The α-$Ni(OH)_2$ is related to the mineral jamborite[19], it too is associated with millerite (NiS) forming a green coating on top of walls and cavities lined by calcite, dolomite and quartz crystals[19]. Mineral samples also show peak broadening when analysed by powder X-ray diffraction, this is attributed to stacking faults in the *c* direction rather than nanoscale particle sizes which also broadens peaks[20]. Elemental analysis of jamborite samples found nickel to be the main metallic component with minor amounts of sulfur, iron and cobalt present. Optical microscopy of samples showed that, under low magnification, the crystals are fibrous and lamella shaped. Lattice parameters were reported to be (hexagonal) a = 3.07 Å c = 23.3 Å[19], similar to the lattice parameters obtained from powder X-ray diffraction analysis of synthetic materials synthesised by Glemser and Einerhand[21].

As shown in Figure 1.7, clear differences between the α and β phase can be observed by analysis of the X-ray diffraction patterns; crystalline β-$Ni(OH)_2$ shows maximum intensity at around 4.6 Å (about 19° 2θ) for the (001) plane, whereas α-$Ni(OH)_2$ has broad reflections at 8.5 Å (about 11° 2θ) and 2.5Å (35° 2θ).

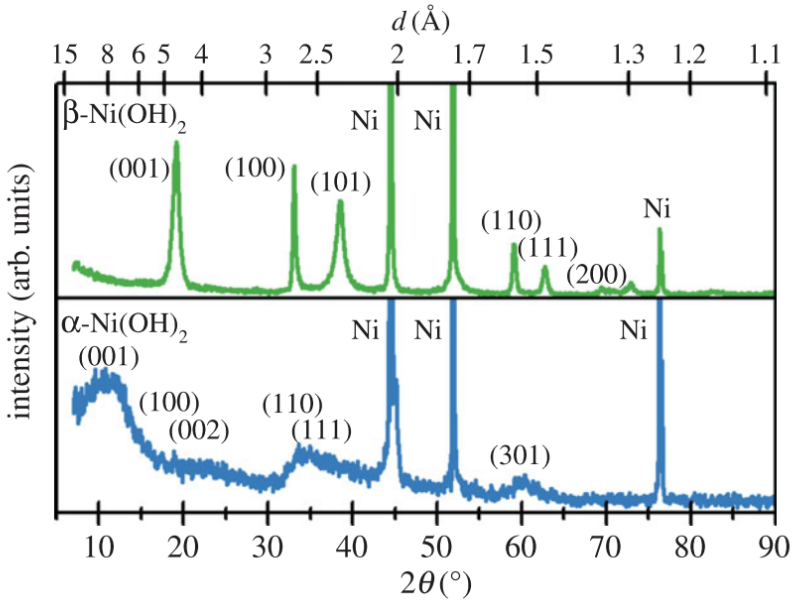

Figure 1.7 - XRD patterns of $Ni(OH)_2$ films deposited on Ni substrates using Cu K_α X-ray source β-$Ni(OH)_2$ (Green), α-$Ni(OH)_2$ (Blue).[7]

The level of crystallinity is higher for β-$Ni(OH)_2$, with α-$Ni(OH)_2$ forming anisotropic broadening as shown in Figure 1.7. A phase which is the intermediate between α-$Ni(OH)_2$ and β-$Ni(OH)_2$ with an interlayer spacing of 5.4 - 5.6 Å, has been reported[22]; this phase will be described in this report as β*-$Ni(OH)_2$. This phase lies between the near-amorphous hydrated structure and the anhydrous crystalline phase thought to be an interstratification of the two species of alpha and beta[20]. Also documented is the existence of badly crystalline beta nickel hydroxide, denoted as β_{BC}-$Ni(OH)_2$[23], which may or may not be related to β*-$Ni(OH)_2$.

1.4.3 Beta nickel oxyhydroxide (β-NiOOH)

Nickel hydroxide is an electrochemically active material and it is important to discuss the higher oxidation states of the nickel hydroxide polymorphs. On charging, β-$Ni(OH)_2$ is converted to β-NiOOH with the removal of a proton and one electron, the structure is not as ordered as β-$Ni(OH)_2$. The *a* parameter of the unit cell decreases

to *a* = 2.82 Å due to the reduced Ni - Ni distances and the interlayer distance increases to *c* = 4.85 Å. This is a result of the increased electrostatic repulsion of the nickel octahedral layers from the removal of a proton[24]. Discharging of β-NiOOH results in transformation back to β- $Ni(OH)_2$, however overcharging of β-NiOOH leads to the formation of hydrated γ-NiOOH.

1.4.4 Gamma nickel oxyhydroxide (γ-NiOOH)

Charging of the α-$Ni(OH)_2$ and overcharging of the β-NiOOH polymorph results in the formation of γ-NiOOH with the proposed structural formula[24] $A_xH_y(H_2O)_zNiO_2$, $x, y \leq 1$ and A = Na^+or K^+. On discharge of γ-NiOOH, the α-$Ni(OH)_2$ structure is reformed. However immersion of the electrode in aqueous alkaline electrolyte will also cause dehydration to form the β-$Ni(OH)_2$ polymorph.

Additionally, overcharging of the β-NiOOH structure is required to maintain high capacity, however this leads to the formation of the hydrated γ-NiOOH polymorph. There is a large change in interlayer distances which increases mechanical stress of the layers resulting in swelling of the material. For this is the reason, the β/β redox couple is used for battery applications as opposed to the α/γ redox couple.

However, it should be noted that use of the α/γ redox couple could bring several benefits, a larger number of exchanged electrons per nickel ion as the oxidation number of the γ-NiOOH phase approaches 3.5[6], reduced damage to the electrode from overcharging the material caused by the β-NiOOH to γ-NiOOH transformation. In addition, a higher diffusion coefficient for protons due to solvent molecules present between the layers of nickel hydroxide / nickel oxyhydroxide, these aspects could improve performance of electrochemical devices.

1.5 Synthesis of nickel hydroxide materials

There are an ever growing numbers of ways to synthesise nickel hydroxide materials stated in the literature, meaning choosing the best method for a given application can be challenging. The resulting type of nickel hydroxide (α or β), crystallinity, morphology (nanostructure / porosity) and bulk form (thin film / powder) is very sensitive to reaction conditions. Reported here is a description of the chemical precipitation and electrochemical deposition methods of nickel hydroxide powders and films.

1.5.1 Chemical precipitation

Dropwise addition of alkaline solutions (for example NaOH, KOH, Na_2CO_3, NH_4OH) to aqueous solutions of nickel (II) salts (or vice versa), sufficient enough to raise the pH of the reaction mixture past the solubility limits of nickel hydroxide, will form chemical precipitates (equation 1.1). The product is typically collected by gravity or vacuum filtration and washed with cold solvents / deionised water.

$$Ni^{2+}_{(aq)} + 2OH^-_{(aq)} \rightarrow Ni(OH)_{2\,(s)} \qquad \text{Equation 1.1}$$

The resulting phase and crystallinity of the product depends on several factors including the base used, the concentration of the reactants, the duration of the reaction, the reaction temperature and the pH of the solution.[25]

Chemical precipitates formed at low temperature[26] typically form α-$Ni(OH)_2$. However, at higher temperatures it will begin to form a β phase. It has been suggested that all precipitates are initially created as α-$Ni(OH)_2$ however rapid ageing occurs to convert the material to a more crystalline form, i.e. that of β-$Ni(OH)_2$.

It is also possible to chemically age α-$Ni(OH)_2$ to form β-$Ni(OH)_2$ if the product is suspended in water for a long time or in a highly concentrated alkaline solution at elevated temperatures.

1.5.2 Electrochemical deposition

Thin films of α, β and mixed α/β nickel hydroxide material can be deposited via electrochemical precipitation on a conductive electrode immersed in a dilute aqueous solution of a nickel salt.[27] This is a multiple step reaction, beginning with the initial reduction of water to form a localised increase of pH at the surface of the electrode via the application of a negative potential (equation 1.2). With the increase of concentration of OH^-, the Ni^{2+} ions in the solution react to form a thin precipitate on the surface of the electrode due to $Ni(OH)_2$ low solubility in water (equation 1.3).

$$H_2O_{(l)} + 2e^- \rightarrow H_{2\,(g)} + OH^-_{(aq)} \qquad \text{Equation 1.2}$$

$$Ni^{2+}_{(aq)} + 2OH^-_{(aq)} \rightarrow Ni(OH)_{2\,(s)} \qquad \text{Equation 1.3}$$

The resulting phase of the nickel hydroxide material is sensitive to reaction conditions, such as; the deposition solution (i.e. whether it is a solution of $Ni(NO_3)_2$, $NiSO_4$ or $NiCl_2$), the concentration of the deposition solution, the cathodic current density applied to the electrode and the temperature at which the reaction is taking place[28]. In addition, only the hydroxide ion is generated electrochemically, the precipitation occurs in much the same way as in the chemical precipitation method. Additionally, the oxidation number of the Ni^{2+} ion is unchanged through the electrochemical synthesis of nickel hydroxide therefore it is dissimilar to the formation of nickel hydroxide through electrochemical oxidation of metallic nickel electrodes when bare nickel metal is oxidised to form nickel hydroxide.

It should also be noted that at low nickel salt concentrations and cathodic currents, Faradic efficiency of the deposition approaches 100%. However, higher concentrations of nickel salts dramatically reduce this to approximately 20% due to the formation of soluble species such as $[NiOH]^+$ and $[Ni_4(OH)_4]^{4+}$, which can diffuse from the electrode surface, retarding precipitation.[29]

1.5.3 Other synthesis methods

There are many other methods of producing nickel hydroxide based materials. Reported here are brief descriptions of the most notable ones from the literature.

Sol gel synthesis - a multistep method where a sol or suspension of nickel (ii) hydroxide particles are created through chemical precipitation then reacted through simultaneous hydrolysis and polycondensation to form a three dimensional network. The material can be aged and dried to form a xerogel, or supercritically dried to form an aerogel. This method can be used to create α or β nickel hydroxide with a variety of morphologies[30,31,32].

Chemical ageing - α-$Ni(OH)_2$ materials spontaneously dehydrate to form β-$Ni(OH)_2$ in alkaline environments[5]. The process is known as chemical ageing and typically performed at high temperatures in concentrated alkaline aqueous solutions. It has been shown that this transition will occur in the original reaction solution, concentrated alkaline solutions at room temperature and in pure water[33].

Hydrothermal / solvothermal synthesis - the synthesis of materials within a heated pressure reactor using water (hydrothermal) between 150 - 200°C typically generates highly crystalline phases of nickel hydroxide. However, it is possible to form alpha nickel hydroxide though the addition of intercalating agents to separate the layered sheets, or through using solvents (solvothermal) as a reaction medium.

Reducing the time or temperature of the reaction also leads to less crystalline forms of nickel hydroxide. The use of hydro or solvo-thermal synthesis routes can also lead to the formation of nanoscale particles of various shapes including nanoflowers, nanoribbons and nanoplates[34].

Surface layers on nickel substrates - when mechanically polished or electro-polished, metallic nickel forms an oxide layer in the presence of air, this layer has shown to consist of non-stoichiometric nickel oxide (such as NiO_x) coated in a thin layer of α-$Ni(OH)_2$. Nickel hydroxide also forms during the corrosion and passivation of metallic nickel or nickel containing alloys[35].

Microwave synthesis - heating a reaction vessel using microwaves is analogous to heating using traditional forms, however the distribution of heat is more even throughout the vessel thus forming a narrower particle size distribution in addition the heating times are greatly reduced. The use of microwaves can also generate nanoscale particles with the addition of intercalating additives[36].

Sonochemical synthesis - Through the use of ultrasonic sound waves, unique morphologies of nickel hydroxide materials can be prepared, this method of synthesis generates the collapse of micro-bubbles in the reaction medium and leads to highly localised temperatures of 5000°K[37].

1.6 Properties of doped nickel hydroxide materials

Studies into the doping of nickel hydroxide (and nickel oxide) materials have been widespread. The main interest was to enhance the performance of the $Ni(OH)_2$/ NiOOH redox couple for use in commercial rechargeable batteries[38,39] . Researchers interested in electrochromic applications have learned from the many structural studies on doped nickel hydroxide conducted on battery electrodes.

Many studies show that a 20% mole replacement of nickel with a trivalent metal ion is the best method to stabilise the α/γ redox couple and structure of a nickel hydroxide thin film or powder[24]. The term "stabilised" is widely used in the literature to describe a method to maintain the α-($Ni(OH)_2$ phase in an open hydrated structure[24]. Stabilised α-$Ni(OH)_2$ will have a different crystal structure to that of freshly deposited un-doped α-$Ni(OH)_2$. This typically causes a corrugated, crumpled structure of the layers as the more positive trivalent cations distort the layer structure electrostatically. Charge balancing anions in the interlayer region stabilise the charge, but also exhibit steric hindrance forcing sheets of nickel hydroxide apart, producing α-$Ni(OH)_2$ like structures. Interlayer ions, water molecules and the nickel hydroxide sheets can form hydrogen bonds. The overall formula can be written as $[M^{2+}_{1-x}M^{3+}_{x}(OH)_2][A_{x/n}{}^{n-}*yH_2O]$, were A are anions inserted into the interlayers. These materials are better described as layered double hydroxide (LDH) with a hydrotalcite like crystal structure[40]. Natural hydrotalcite minerals are most stable where the dopant level of the trivalent metal is either x = 0.33 or x = 0.25. These x values mean trivalent metal ions are completely surrounded by divalent cations[24] and so the stability is enhanced as shown in figure 1.8 below.

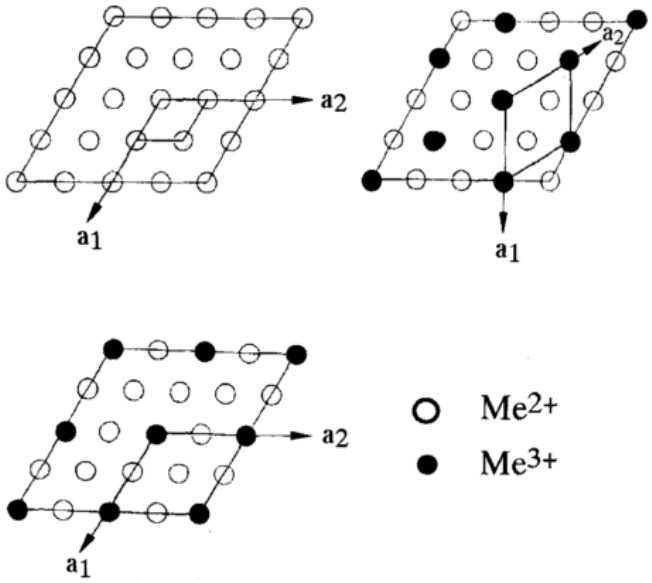

Figure 1.8 - Me^{2+} (divalent metal) and Me^{3+} (trivalent metal) distributions within the octahedral layers[24] in (0,0,1), basel axis are indicated (top left) brucite, (top right) 2:1 hydrotalcite (bottom left) 3:1 hydrotalcite.[24]

1.6.1 Cobalt doped nickel hydroxide

Cobalt (ii) has been used as a dopant since the time of Thomas Edison's nickel-iron battery. Its addition is common along with zinc in battery applications[1,24]. The following battery application[41] study proposed a mechanism for improvements to nickel hydroxide systems via the addition of cobalt.

A 10 % weight addition of divalent cobalt (II) oxide powder was made to a nickel hydroxide battery electrode, forming a blue Co (II) complex, upon electrochemical charging the $Co(OH)_2$ (II) irreversibly transformed into CoOOH (III), incorporating a highly electrically conductive matrix through the nickel hydroxide electrode as summarised in the schematic in figure 1.9.

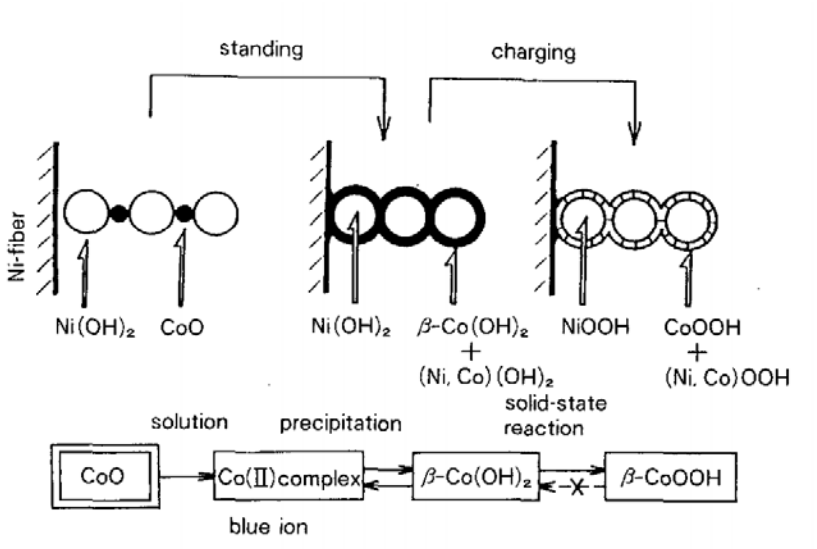

Figure 1.9 - Assumed mechanism of effect of cobalt addition and irreversible conversion of cobalt (II) oxide to cobalt (III) oxyhydroxide[41]

X-ray absorption spectroscopy studies suggests that, incorporated cobalt ions are trivalent[42] regardless of the oxidation state of the nickel ion in 10% doped cobalt nickel hydroxide films. EXAFS showed that bond distances between nickel and cobalt ions matched those of nickel – nickel bonding distances of pure nickel hydroxide thin films. This suggests that cobalt is incorporated into the nickel hydroxide forming a single phase solid solution. Corrigan however suggested that cobalt can occupy either the octahedral (Ni^{2+}) sites or inter-planar spaces between the octahedral sheets[43] (figure 1.10). It has also been reported that the addition of cobalt to nickel hydroxide electrodes reduce the average oxidation potential[44], increasing the range between the nickel hydroxide oxidation peak and the decomposition of electrolyte in a cyclic voltammogram improving the electrodes durability.

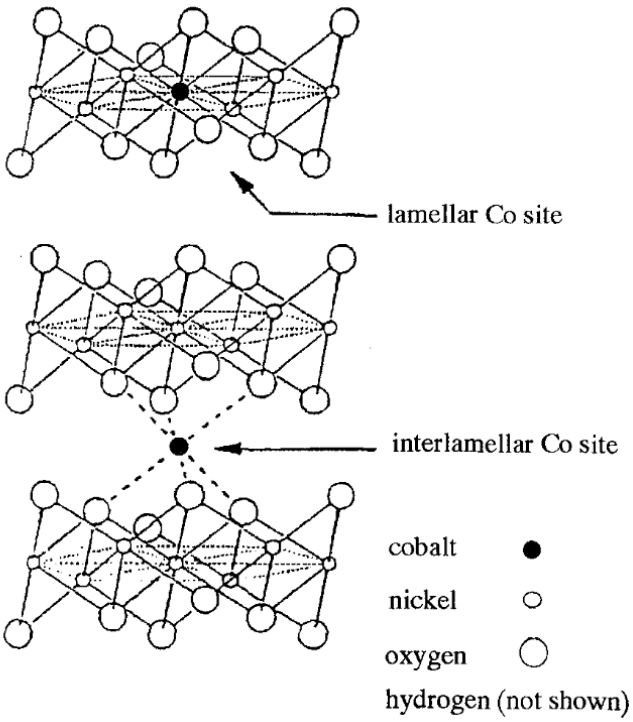

Figure 1.10 - Possible sites of cobalt ions in nickel hydroxide.[24]

Research by Tarascon[45], in an attempt to better understand the electrochemistry and impact of the $Co(OH)_2$ / CoOOH reaction, suggested that generation of highly conductive tetravalent Co IV was formed with faster charging rates (C/5) causing the mosaic $Co_x^{4+}Co_{1-x}^{3+}OOH_{1-x}$ phase to form. At slower charging rates (C/100), Co^{2+} can dissolve into the electrolyte, reducing the conductivity of the electrode leading to CoOOH.

It was demonstrated by Kamath[46] that the introduction of cobalt ions into nickel hydroxide electrodes increased the reversible discharge capacity of β-$Ni(OH)_2$. However this increase was not observed for β_{BC}-$Ni(OH)_2$ or for α-$Ni(OH)_2$. This suggest that the addition of cobalt at the studied levels does not stabilise the α → β transition. It was proposed that two mechanisms could be responsible for these results, cobalt incorporation in the nickel hydroxide lattice and / or the formation of highly conductive H_xCoO_2 ($x < 1$). From XRD analysis of the spent electrodes, it was

shown that the structure of the material. Therefore the increase in performance was purely due to the introduction of a conductive matrix. It was noted by the author, that graphite, which is also an additive in some battery electrodes, also improved the electrical conductivity of the material, however it is not as effective as cobalt. Graphite undergoes intercalation, and provides conductive networks between macroscopic particles. Cobalt however experiences a dissolution / re-precipitation process which creates conductive pathways on an atomic level. However, nano-structured carbon allotropes (graphene, carbon nanotubes) incorporated into nickel hydroxide electrodes[47] have shown ultra-high performance levels.

An electrochromic study by Corrigan[48] showed that nickel hydroxide films on fluorine doped tin oxide (FTO) glass substrates (approximately 30 nm thick) displayed high levels of degradation after 500 electrochemical cycles (0.0 V ↔ + 0.6 V Vs Hg/ HgO). The coloration had decreased slightly, however bleaching was dramatically affected by the aging process as shown in figure 1.11.

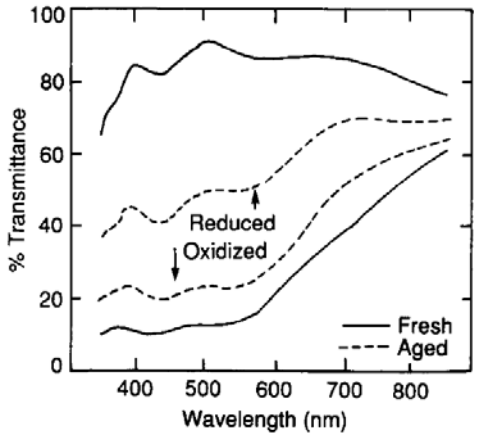

Figure 1.11 - Spectra of a nickel hydroxide electrode in reduced (bleached) measured at 0.0 V and oxidised (coloured) state measured at + 0.6 V. [48]

A 10% molar replacement of nickel (II) ions for cobalt (II) ions in the 0.01 M metal nitrate deposition solution showed improved stability of the thin film measured over

500 electrochemical cycles. It should be noted that the nickel cobalt hydroxide electrode was treated with hot water and placed in a beaker with 95°C water for 30 minutes. This is to convert the electrochemically deposited α phase to β typically found in batteries. Figure 1.12 shows the continual decrease in transmittance of the bleached state as the number of electrochemical cycles increase, other results (not displayed) showed a shift in potential at which bleaching occurred and a decrease in capacitance of the electrochemical switching after 50 cycles. The decrease in performance of the electrodes are more dramatic during the first 50 cycles. The subsequent 450 cycles show a more gradual decrease in performance.

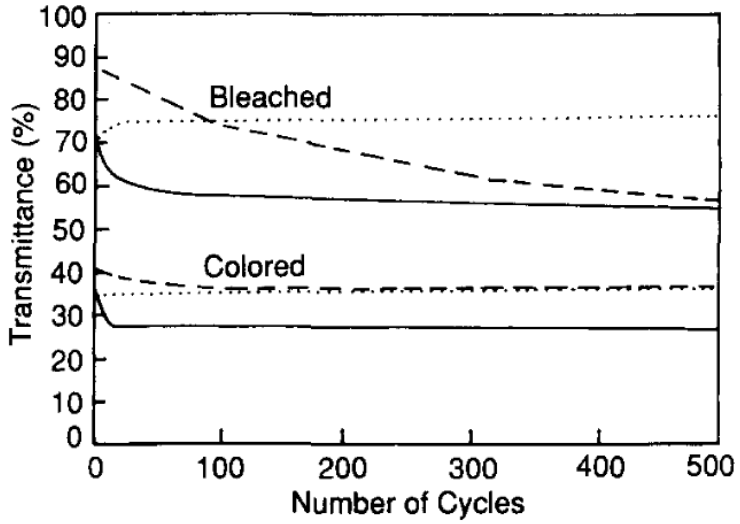

Figure 1.12 - Optical transmittance at 500 nm of coloured and bleached electrodes as a function of the number of electrochemical cycles. Nickel / cobalt hydroxide electrode (solid line), nickel / cobalt / lanthanum hydroxide electrode (dotted line) and un-doped nickel hydroxide (dashed line).[48]

Stability of the charge and discharge characteristics of the heat treated nickel cobalt binary electrode were an improvement, according to the author, on heat treated un-doped nickel hydroxide thin films. However, as observed by Corrigan, the transmittance level of the bleached state (less than 60% after 100 cycles) would be

unfit for electrochromic window applications. In the same study, a ternary electrode of nickel / cobalt / lanthanum (90% / 5% / 5%) showed durable electrochromic performance for at least 2000 cycles suggesting a synergistic effect from the dopants.

Electrochemically co-precipitated thin films of nickel hydroxide[44] with target ion. compositions of 5% and 10% mole replacement of nickel with cobalt, zinc and cadmium elements, typically found in combination with nickel hydroxide for battery applications, were studied[44]. Elemental analysis, using ICP-AES, of the Ni/Co deposition solutions showed that the solutions contained 4.2 % ± 0.2%, and 9.6 % ± 0.5% of cobalt (after the deposition process), and as deposited films showed 5% ± 1% (5% target) and 6% ± 1% (10% target) respectively. Departure from the target Co levels in the solutions were put down to error in chemical manipulation of solutions and levels of hydration from precursor salts. However deviation of the thin film composition was shown to be attributed to the solubility products (K_{sp}) of the various hydroxides. $K_{sp}[Ni(OH)_2] = 5.47 \times 10^{-16}$ and $K_{sp}[Co(OH)_2] = 5.92 \times 10^{-15}$, as the K_{sp} of the additive is bigger than the nickel, the nickel hydroxide is precipitated preferentially on the surface of the electrode.

Atomic force microscopy (AFM) maps of the 6% cobalt nickel hydroxide electrode was compared to an un-doped nickel hydroxide electrode (figure 1.13). A homogenous thin film was observed suggesting strong physical interactions of the lattice structure, implying a solid solution with cobalt atoms occupying nickel sites in the crystal structure and not two separate phases. The ionic radii of Ni^{2+} (0.69 Å) and Co^{2+} (0.67 Å) are similar and the metal - oxygen bond strengths for the two species are also very similar (382.0 KJ mol^{-1} for Ni-O and 384.5 KJ mol^{-1} for Co-O).

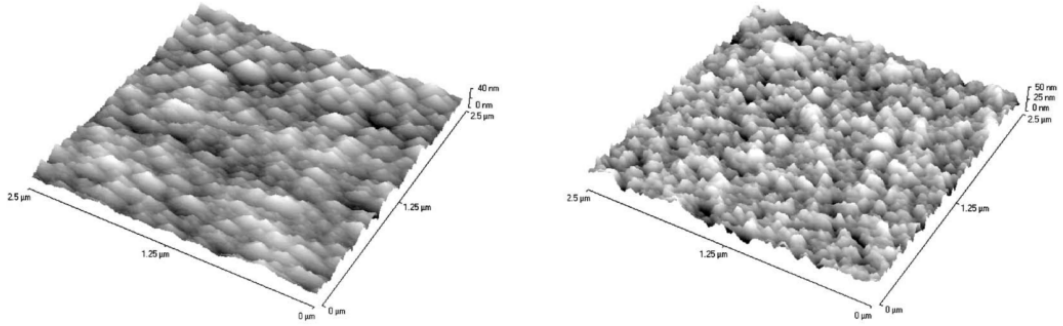

Figure 1.13 - AFM image of 2.5 x 2.5 µm area, as deposited on indium tin oxide substrates (left) un-doped nickel hydroxide (right) nickel hydroxide 6% cobalt hydroxide.[44]

Cyclic voltammetry showed that the co-precipitation of cobalt ions improved the reversibility of the electrode compared to the unmodified nickel hydroxide electrode. In addition, the highest performing electrode for cycle life was doped with cobalt ions, after 200 charge discharge cycles the electrode retained 10% of its initial capacity. Spectroelectrochemical data showed that colour change was shifted to less positive potentials (figure 1.14). As mentioned previously, it was observed that the addition of cobalt reduced the optical contrast of the thin film.

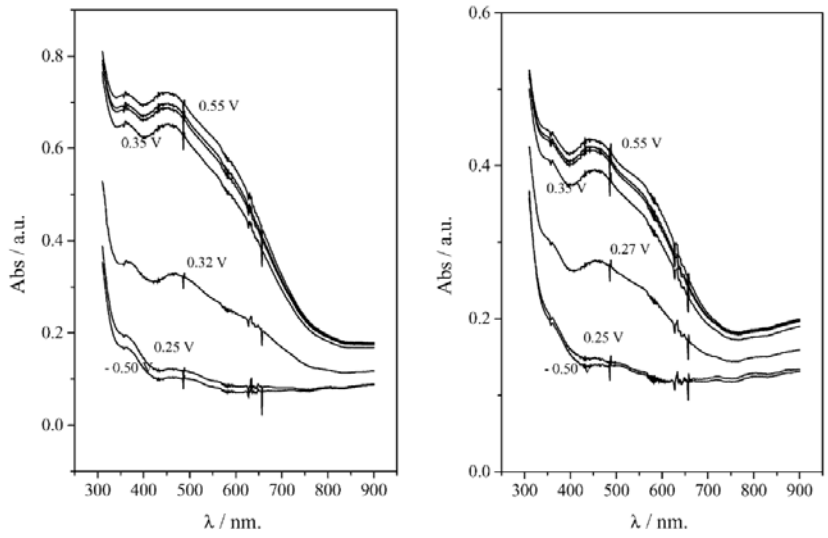

Figure 1.14 - Spectroelectrochemical measurements of (left) nickel hydroxide electrode (right) nickel hydroxide electrode 6% cobalt hydroxide electrode.[44]

1.6.2 Cadmium and Zinc doped nickel hydroxide

Cadmium and zinc are common additives in alkaline batteries with zinc replacing cadmium for use in rechargeable batteries due to environmental and health concerns[10]. It has been reported in the literature[49,44] that cadmium and zinc increase the oxidation over-potential of the oxygen evolution reaction. These elements have been added to batteries in order to prevent the formation of the γ-NiOOH polymorph and improve reversibility of the electrode by maintaining the β/β redox couple.

AFM images[44] suggest that zinc and cadmium, unlike cobalt, do not form a solid solution when deposited with nickel hydroxide, the atomic radii of divalent zinc (0.74 Å) and cadmium (0.97 Å) are much larger than that of Ni^{2+} (0.69 Å).The metal oxygen strengths are also weaker, 270.7, 235.6, 380.0 KJ mol^{-1} for Zn-O, Cd-O and Ni-O respectively. These AFM images (not shown) show a higher active area with an increase in the number of peaks and troughs on the electrodes surface, this open

structure can increase the proton diffusion co-efficient thus leading to changes in the electrochemical response in terms of charge/ discharge behaviour[50].

An electrochemical study of zinc substituted nickel hydroxide by Delmas[51] demonstrated the complexity of electrochemically cycling zinc nickel hydroxide composite electrodes. Described are several simultaneous processes with some that occur in the solid state and others involving a dissolution step. These processes increase the stability of the β/β redox couple. It was also shown that stabilisation of the alpha phase occurs when nickel ions are replaced with 20 – 50 molar % zinc.

1.6.3 Manganese doped nickel hydroxide

A study of the structural properties of manganese substituted nickel hydroxides conducted by Delmas[52,53] et al, showed that a 20% mole or greater replacement of trivalent manganese stabilised the α-$Ni(OH)_2$ phase. The report suggested that other studies which used Mn^{2+}, but did not carry out a pre-oxidation step, still used the 3+ state of manganese as untreated solutions turned from green to brown in colour over the course of 15 hours.

Samples of $Ni_{(1-y)}Mn_y(OH)_2$, where Mn replacement ranged from y= 0.1 - 0.4 were synthesised and characterised before and after aging in 5 M potassium hydroxide solution for one day and one month. XRD and FTIR data collected on the samples were compared to that of un-doped β-$Ni(OH)_2$. For the un-substituted system, $d_{(001)}$ = 4.6 Å (interlayer spacing) and $2d_{(110)}$ = 3.10 Å (equivalent to inplane metal – metal distance). However for $y \geq 0.2$ α-$Ni(OH)_2$ was formed which crystallised in rhombohedral space group R-3m. The interlayer d - spacing for y=0.3 (now $d_{(003)}$) = 7.8 Å ($c_{hex./3} = d_{(110)}$) and the metal-metal spacing maintained $d_{(110)}$ = 3.1 Å. The 7.8 Å interlayer distance was attributed to intercalations of carbonate ions and water

molecules between the layers. CO_3^{2-} anions were present to compensate for the excess positive charge of Mn^{3+} however, in this report it does not explicitly state where the anions were sourced. Most likely the carbonate was formed via aborbed CO_2 from the air as the reaction was carried out in an open system with a high pH and high concentration.

Ageing studies in 5 M potassium hydroxide showed that little structural change was observed after one day, however after one month major structural changed were observed. The (003) and (006) peaks transformed into a single broad asymmetric reflection (*d* = 4.3 Å) which suggested interstratifications of the material as shown in figure 1.15 below.

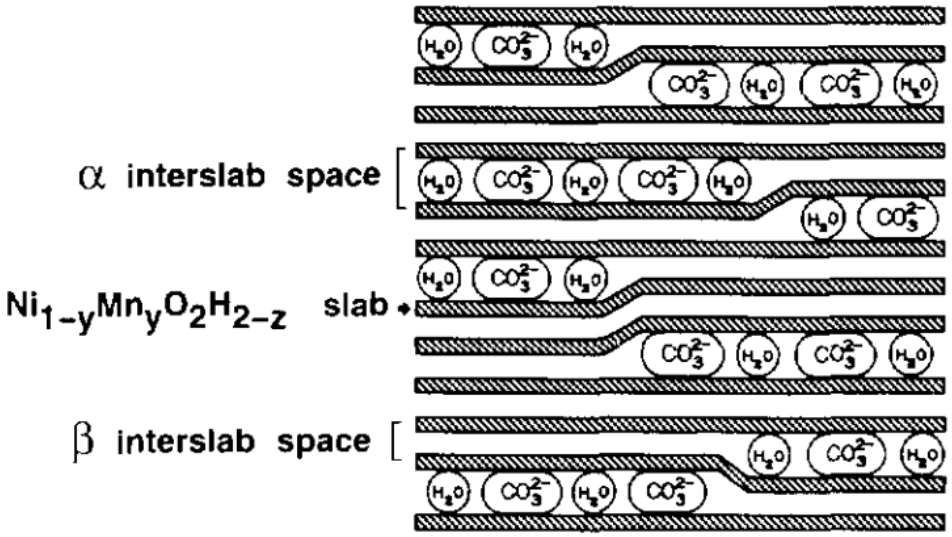

Figure 1.15 – Schematic representation of an interstratified structure constituted of α and β-type interslab spaces.[53]

FTIR also supported the results obtained by PXRD on samples which had been aged, as after one day in alkaline solution the sample was found to be α-$Ni(OH)_2$ with broad bands in the region of 3400 cm^{-1}, whereas after one month a sharp band

at 3650 cm^{-1} appears, and the $v_3(CO_3^{2-})$ band at 1360 cm^{-1} is reduced. This suggests an increase in the presence of the beta phase at the expense of the alpha phase.

Iodometric titration was used to determine the average oxidation state of the nickel and manganese ions in the freshly precipitated material and the day and month aged samples. Data suggested that manganese ions are typically in the trivalent state for fresh material, oxidising to the tetravalent state on aging in the alkaline solution. This was supported by evidence from magnetic susceptibilities measurements of the fresh α-$Ni(OH)_2$ and month aged interstratified sample showing unstable manganese transforming from the trivalent into the tetravalent ion during the phase change.

The structural analysis of manganese substituted α and β $Ni(OH)_2$ was published in 2008 by Sakai[39], with the use of high energy synchrotron light it was possible to perform XAFS and high resolution XRD analyses. 10% (figure 1.16) and 20% (figure 1.17) mole replacements of manganese in nickel hydroxide electrodes showed cycling between the β/γ and α/γ polymorphs respectively. The location of the manganese ions were only on the nickel sites for the 10% substituted electrode whereas for the 20% substituted nickel hydroxide the manganese could be found on the nickel sites and in between the interlayers; the manganese in the interlayer spacing were responsible for stabilising the α-$Ni(OH)_2$ phase. Using a two phase model[54] of nickel hydroxide (ideal phase and fault phase), structural refinement was possible, fault phases could be identified by the shift of the nickel atoms and higher proportion of potassium ions and water molecules intercalated between the layers.

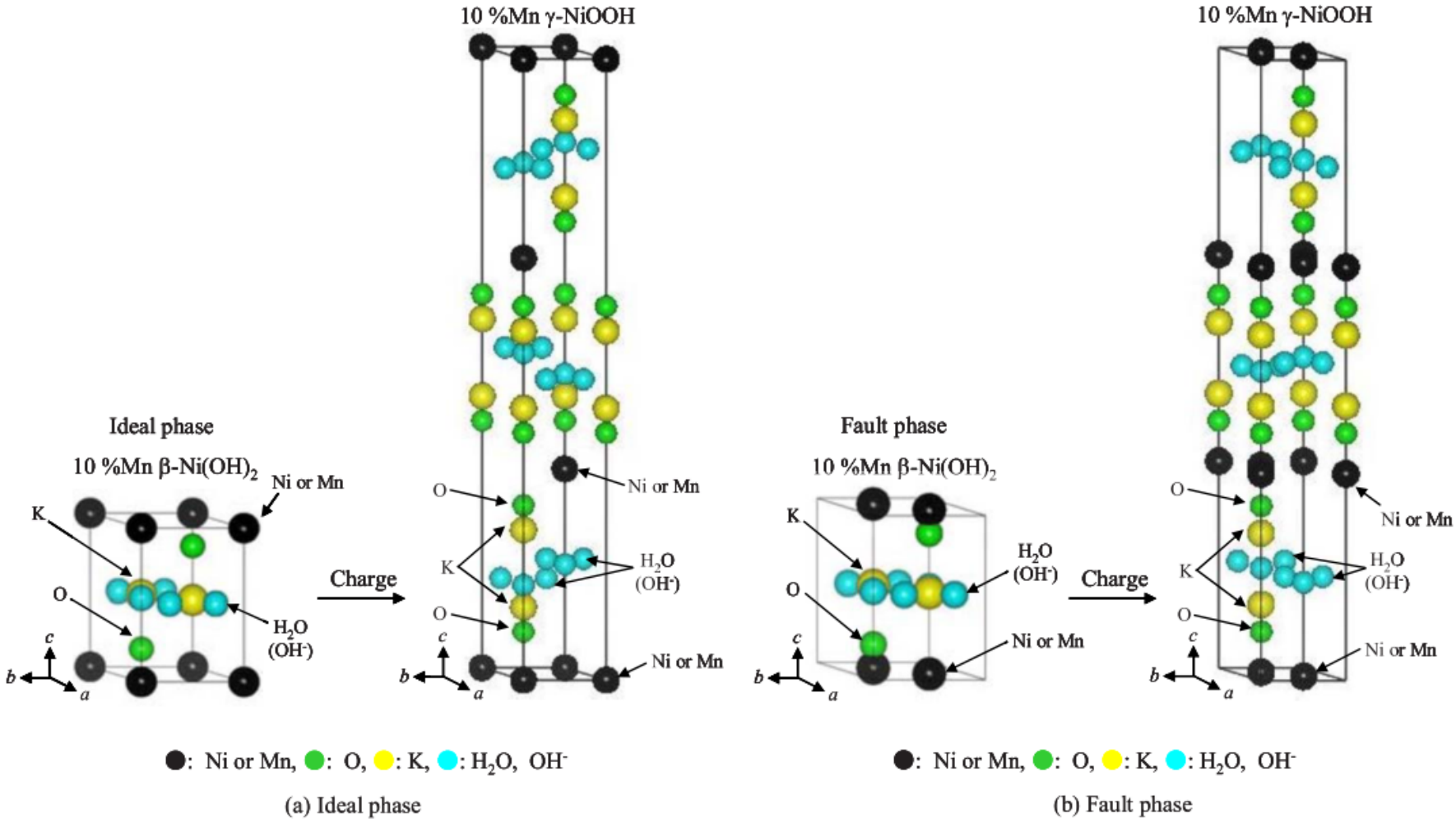

Figure 1.16 - refined structure of (a) ideal phases and (b) fault phase of 10% Mn β-$Ni(OH)_2$ and 10% Mn γ-NiOOH.[39]

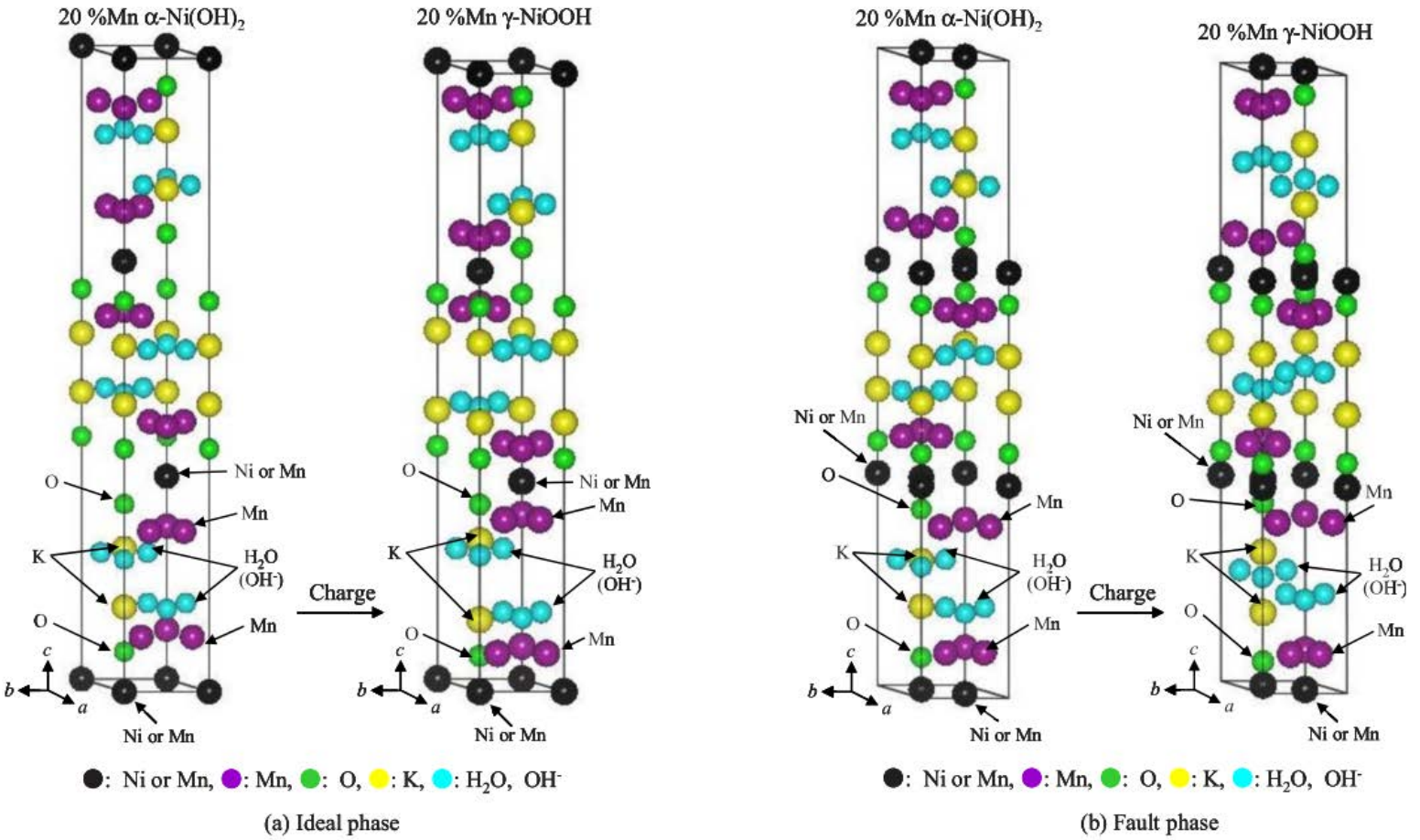

Figure 1.17 - Structure of (a) ideal phases and (b) fault phases of 20% Mn α-$Ni(OH)_2$ and 20% Mn γ-$Ni(OH)_2$.[39]

1.6.4 Iron doped nickel hydroxide

The addition of iron ions to nickel hydroxide powders clearly show the stabilisation of the α-$Ni(OH)_2$ phase[55, 56]. However, it was demonstrated that contaminant iron ions from glassware in nickel hydroxide electrodes promote the oxygen evolution reaction (OER) [49,56]. Due to its higher peak oxidation potential which is linked to the tetravalent iron ion, battery and electrochromic applications have not adopted this additive. Nickel iron hydroxide films are still researched for their water splitting applications[15]. The role of iron in the enhanced OER activity is not yet fully understood, nevertheless it has been shown that ultra-pure nickel hydroxide electrodes are a poor catalyst for oxygen generation in basic media[57]. Corrigan showed that as little as 1 ppm of iron as ions present in the electrolyte will have an effect on the electrochemical properties of the thin film[58].

In a study published in 2000[59], thin films were analysed using XANES and EXAFS to investigate the local structure of iron doped nickel hydroxide thin film. Cathodic electrodeposition of solutions containing Fe(II) and Ni(II) ions resulted in iron occupying nickel crystal sites in α-$Ni(OH)_2$. The XANES showed that iron in the film was trivalent, and Fe-O and Fe-Ni bond distances were 2.00 Å and 3.11 Å respectively. The Fe-O bond length was too small for $Fe(OH)_2$ (2.10 Å) however the distance was in good agreement with the metal oxygen bonding of γFeOOH. It was found that the Fe-Ni bond distance was in accordance with Ni(II)-Ni(II) bonding found in α-$Ni(OH)_2$. During anodic oxidation, the XANES analysis showed that the iron energy shifted to higher values, which suggested an increase in oxidation state. On charging, the Fe-O bond length was shortened to 1.94 Å and the Fe-Ni bonding was reduced to 2.84 Å. The study found that the iron nickel bond length was in good agreement with modelled Ni(IV)-Ni(IV) bonding distances in γ-NiOOH[59]. The Fe-O

bond length was shown to be similar to that of iron in $SrFeO_3$ suggesting a tetravalent iron ion was incorporated into the film[59]. The group suggested that iron in the oxidised film was tetravalent but the metal oxygen bond still exhibited a high level of covalent bonding.

1.6.5 Aluminium doped nickel hydroxide

Aluminium doped nickel hydroxides are reported to be more stable than cobalt or iron doped nickel hydroxide materials[24]. Additions of aluminium[60] have shown to improve the stability of the α/γ redox couple but not permanently. A structural study showed that nickel hydroxide with 20% (figure 1.18) of the metal ions substituted by aluminium showed the α-$Ni(OH)_2$ / γ-NiOOH phase transformation during the charge and discharge process. The use of synchrotron X-rays made it possible to carry out a structural refinement of the ideal and fault phase of nickel hydroxide from high resolution powder XRD data. Aluminium ions were found to situate in both nickel and interlayer sites of the lattice, however it was found that the stabilised α phase would be transformed to the β-$Ni(OH)_2$ phase after 50 electrochemical cycles as trivalent aluminium migrated from the bulk to the surface of the electrode.

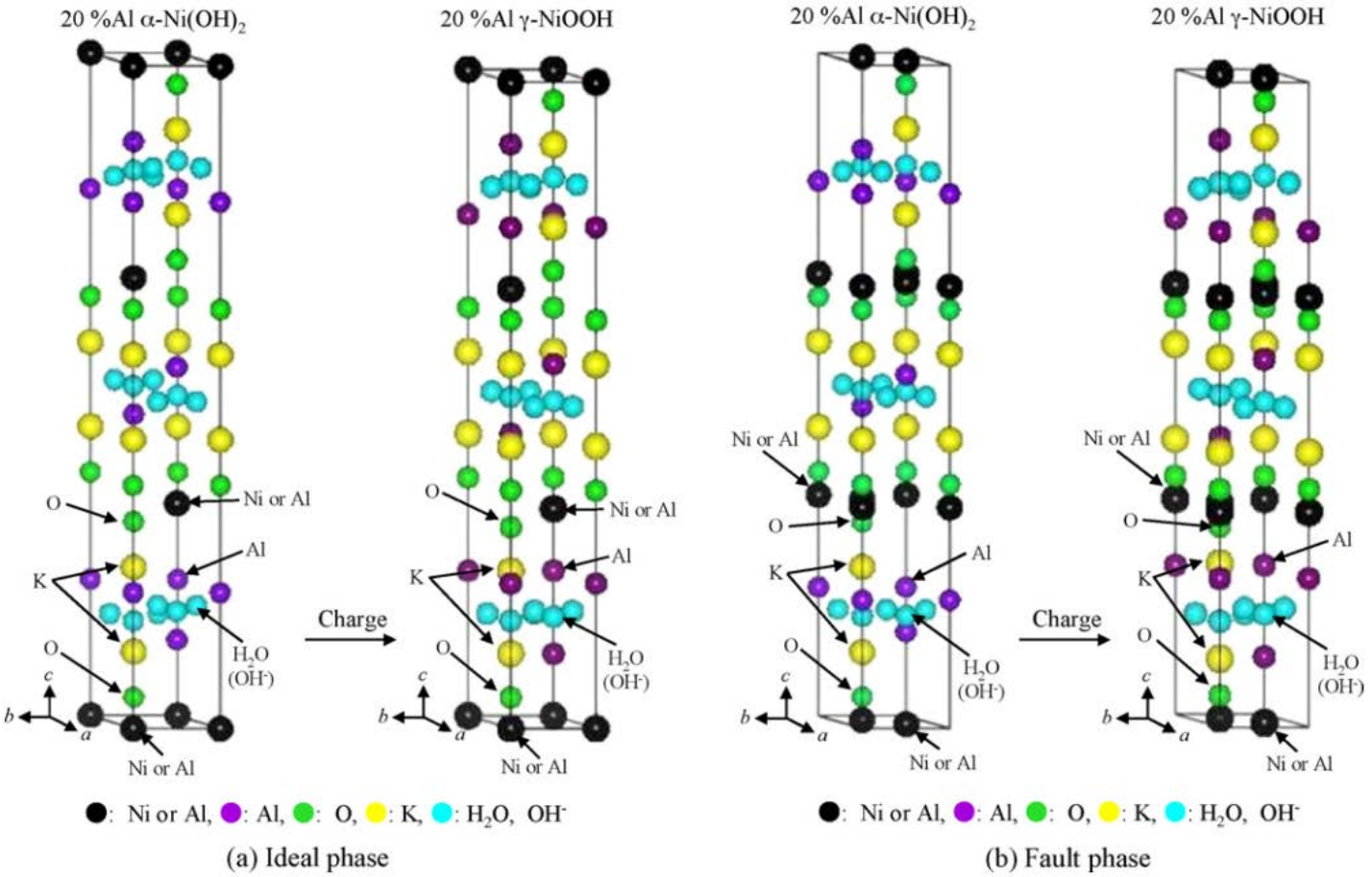

Figure 1.18 - Structural models of the ideal phases and the fault phases of 20% mole Al α-$Ni(OH)_2$ and 20% mole Al γ-NiOOH.[60]

On charging, aluminium that had substituted onto the nickel sites did not migrate, however those in the interlayer position were able to migrate to the edges of the electrodes during electrochemical cycling. Phase transformation from the α-$Ni(OH)_2$ to the γ-NiOOH showed a decrease in the *a* and *c* parameters due to the decrease in the ionic radius of Ni^{2+} (0.69 Å), Ni^{3+} (0.56 Å) and Ni^{4+} (0.48 Å) on the nickel sites.

1.7 Electrochromism and electrochromic applications

As described previously, nickel hydroxide thin films exhibit a colour switching phenomenon known as electrochromism. The term electrochromism defined by Monk, Mortimer and Rosseinsky "is a change, evocation or bleaching of colour as effected by an electron-transfer (redox) process or by a sufficient electric potential. In many applications it is required to be reversible." [61] In this sections, key concepts of electrochromic materials will be outlined and their applications in the real world.

This area of science combines research fields from electrochemistry, organic and inorganic synthesis and spectroelectrochemical techniques such as *in situ* UV-vis spectrometry in order to link chemical structures with their electrochemical performance and optical kinetics.

The term electrochromism is not to be confused with other light modulating technologies such as suspended particle devices (SPD), polymer dispersed liquid crystals (PDLC) or micro-blinds, these technologies are now also referred to as "smart glass / windows/ films", a term which was reserved for electrochromic devices.

1.7.1 Electrochromic theory

The term electrochromic is used to describe a material or device which exhibits electrochromism. For a material, the electrochromic layer must be electroactive and

be able to undergo a redox reaction, either the uptake of electrons (reduction) or the release of electrons (oxidation) as represented below in equations 1.4 and 1.5. The electroactive material must be in contact with an electrode and electrolyte to transfer an electron.

$$\text{Oxidised} + e^- \rightarrow \text{Reduced} \qquad \text{Equation 1.4}$$

$$\text{Reduced} - e^- \rightarrow \text{Oxidised} \qquad \text{Equation 1.5}$$

An electrochromic device may contain one, or more commonly, two electrochromic layers supported on transparent conducting electrodes, separated by an electrolyte which will be described in more detail in a following section.

Contrast Ratio, CR, (equation 1.6) is a measurement used to describe the intensity of the colour transition between one or multiple colour states. Where CR denotes contrast ratio, R_x is intensity of light reflected in the coloured state and R_0 is the intensity of light reflected from a non-shiny (glossy) white card. The specific wavelength (λ_{max}) measured should be specified when reporting CR. The larger the value, the greater the increase in contrast between coloured and bleached states.

$$CR = \left(\frac{R_0}{R_x}\right) \qquad \text{Equation 1.6}$$

Response time, τ, is the time required for an electrochromic device to transition from its bleached to coloured state, or vice versa. In most cases the response time for the bleach to colour and colour to bleach are not equal. It should also be noted, that in the literature there is not a standardised measurement for response time and the parameters are typically denoted by the experimenter for a given application. This makes it difficult when comparing response times of different devices from different studies. For example the response time could be a measure of the time taken for the

absorption of a fraction of colour (90%) at a given wavelength or it could be the time required for a material to accept a given charge to reach a transmission level. In many cases, electrochromic applications in architectural applications do not require a fast response time. A transition between 5 - 10 minutes is preferred as the experience of sudden light fluctuations can be nauseating. Electrochemical devices are not typically used in display devices with high refresh rates (speed of changing an image) due the inability to transition quickly compared to other display technologies.

Write-erase efficiency is the ratio of contrast in which the material is able to fully transition from fully coloured to fully bleached transition. Cycle life is an extension of this, as it is a measure of the number of cycles achieved before significant degradation of the electrochromic performance is observed. Again, there is no specific way to measure this, however researchers look to the field of battery science to assess the performance of shallow and deep charging cycles. Typically, in architectural applications the installations need to be functional for a minimum of 20 years to make them cost effective, this can be equivalent to roughly 10,000 charging cycles.

Colouration efficiency, η, is the amount of colouration formed when a charge is applied to an electrochromic active material / redox pair (equation 1.7). Where *Abs* is measured at the highest absorption wavenumber (λ_{max}) of the system for a given charge (*Q*). A graph of Abs vs. Q gives η as the gradient.

$$Abs = \eta Q \qquad \text{Equation 1.7}$$

As electrochemical devices require two electrochromic active electrodes, they can have complementary colour switching if one is coloured during oxidation and the

other is colourised during the reduction. A common pairing is the use of tungsten trioxide and nickel oxide, in such a system the tungsten trioxide goes from a pale yellow colour to an intense dark blue layer during reduction. On the opposite side of the cell, nickel oxide goes from near colourless to dark brown during oxidation. Because the tungsten trioxide is more intense colour, it is known to be the primary electrochrome, whereas the nickel oxide layer is called the secondary electrochrome.

When one electrochromic layer is able to exhibit more than one electrochromic transition this is known as electropolychromism. Each colour is exhibited at different applied potentials, examples include methyl viologen and prussian blue thin films.

1.7.2 Electrochromic materials

There are many electrochromic active materials. They can be categorised in many different ways, inorganic, organic, etc. However, early on in the field of electrochromism, the type of electrochromic material was defined by the physical state of the electrochrome during colour switching cycles.

Type I The electrochromes remain dissolved in their solvent in both bleached and coloured states. Examples include aqueous methyl viologen and or any viologen soluble in water. In addition phenathiazine (such as methyl blue) in a suitable solvent.

Type II The electrochromes are soluble in the bleached state, but become solid precipitates in their coloured state. Examples of these types of materials include; cyanophenyl paraquat in water. Other examples include viologens with large substituent groups such as heptyl and benzyl viologens which precipitate in their

coloured state. Another type II electrochrome is bismuth metal which can be cyclically precipitated and stripped from an electrode.

Type III These electrochromes remain solid in both bleached and coloured states. The majority of inorganic electrochromes are type III solid state. These are usually contain d-block metal oxides where a small cation (H^+, Li^+) can be transported causing a metal ion to change oxidation state, switching from bleached to coloured states due to the change to the electron charge transfer band of the metal / molecule. Other types of solid state electrochromes include metal hexacyanometallates such as Prussian blue. Organic type III electrochromes are usually conjugated conductive polymers such as poly(3,4-ethylenedioxythiophene) polystyrene sulfonate known as PEDOT:PSS.

1.8 In situ electrochemical cells

An electrochemical cell is a reaction vessel in which electrochemistry can be performed typically with a potentiostat and a 3 electrode set up. An *in situ* electrochemical cell allows for electrochemical species to be characterised by another spectroscopic or diffraction technique while under potential control. This is also known as a spectroelectrochemical cell when a spectroscopic technique is applied to characterise a material.

Both electrochemical performance and measurement technique need to be taken into consideration when a cell is designed. This typically means that a compromise is made in the geometry of the electrodes, the materials used and methods employed to collect data. In section 1.8.1, critical components of an *in situ* electrochemical cell are briefly summarised.

1.8.1 Electrochemical cell components

Working electrode

Working electrodes come in a wide range of shapes, sizes and materials, however for practical and experimental reasons they should be made as small as possible in comparison to the counter electrode. Their function is to study the material or redox reaction of interest. They should not react chemically with solvents or electrolytes used in the experiment and so typical materials used include glassy carbon or inert metals such as gold, platinum or palladium. Preferably the working electrode should have an even current and potential distribution, designed in such a way that all points are geometrically equal distance from the counter (secondary) electrode.[62]

However for working electrodes used in spectroelectrochemical experiments, for example, it is usually a requirement for the working electrode to be electrically conductive and transparent. This requires either a supporting substrate of thin glass or plastic coated in a transparent conducting oxide (TCO) in order to be compatible for UV-Vis type experiments. Examples include fluorine doped tin oxide (FTO), indium tin oxide (ITO) or aluminium doped zinc oxide (AZO). For the best results, it is important that the working electrode surface is thoroughly cleaned of inorganic salts and organic greases are removed prior to its use. This can be achieved through repeated washing with surfactant solutions, water and solvents, sonication in a variety of aqueous and organic solvents or through plasma etching.

Counter electrode

A counter electrode is used to supply the current to the working electrode via the electrolyte, it is designed in such a way that it does not limit the current available to the working electrode. One of the reasons it is preferential that the counter electrode

surface area is much larger than the working electrode. Like the working electrode it too should not react chemically with solvents or electrolytes.

The design of the counter electrode is important in spectroelectrochemical experiments as its position can block the transmission of light through the cell. Typically there is a compromise made between the best geometry for electrokinetics and light absorption through the cell.

Reference electrode

The function of a reference electrode is to maintain a fixed electrochemical potential so that a potentiostat can apply or measure the potential difference between the working electrode and the reference. As the reference electrode acts as a stable half-cell, deviations of the current would be a result of the redox reactions occurring at the working electrode. The reference electrode acts as a point of reference for the reaction to occur. The potential difference of these half cells, compared to normal hydrogen cells, are well known in literature and reference electrodes can be easily calibrated to ensure the that they are functioning within their desired range. Due to size or geometric constrains, a luggin capillary, a small hollow tube positioned between the reference electrode and the working electrode may be required, so that the reference electrode does not have to be physically next to the working electrode but experiences the same electrochemical environment. It is possible also to use an inert metal wire as a quasi-reference if the electrode configuration is highly restricted which can then be cross referenced with a more typical reference electrode.

Electrolyte

The electrolyte is the liquid medium which allows passage of ions and charge between electrodes, it will consist of an aqueous or organic solution with a high concentration of ions and may or may not contain the electrochemically active material under study. The high concentration of salt acts as a supporting electrolyte reducing the resistance between the counter and working electrode and maintaining a uniform current / potential distribution. In most cases the electrolyte will need to be purged with an inert gas such as nitrogen or argon to displace the dissolved oxygen which can have an effect on the experiment through the generation of oxygen gas at the electrode surface at sufficient potentials.

Cell body

The cell body is what holds electrodes in position and the vessel to hold the electrolyte. In many cases an electrochemical cell is made from glass (or quartz) due to its inertness and transparency. However many spectroelectrochemical cell designs can be complex and glass can be difficult to form and seal. Inert polymers (PTFE, or nylon) and metals (stainless steel) can be used instead to create the cell body which are easier to machine. In many spectroelectrochemical designs the cell body is assembled in many parts, it is important that positioning of electrodes do not cause short circuits within the cell and that the cells geometry allows the electrochemistry to occur and the experiment to be able to detect this electrochemistry. This may require the window material to act as an electrode. It is also impetrative that the cell body can be securely and evenly sealed to prevent leaks of the electrolyte solution.

1.8.2 *In situ* electrochemical cell examples

The following section gives several examples of *in situ* spectroelectrochemical cells designed for the use in synchrotron X-ray techniques. All have required components present as mentioned previously, however the materials used and geometries of the electrodes differ depending on the application. It is important to take note that the benefit of *in situ* electrochemical cells is that the material can be studied under potential control giving a more realistic and real-time analysis of how materials function during operation, this contrasts to *ex situ* analysis, which involves removing materials from the system to study their properties, and being less representative of the cell in action.

The cell design in figure 1.20 is simple and would be easy to fabricate. Its gold coated mylar window would be effective for measuring the XAFS however would not be suitable to use in situ UV-Vis studies in transmission. However with the “U” shaped gasket and only 4 screws holding the cell together their could be a risk of leaks or spillages.

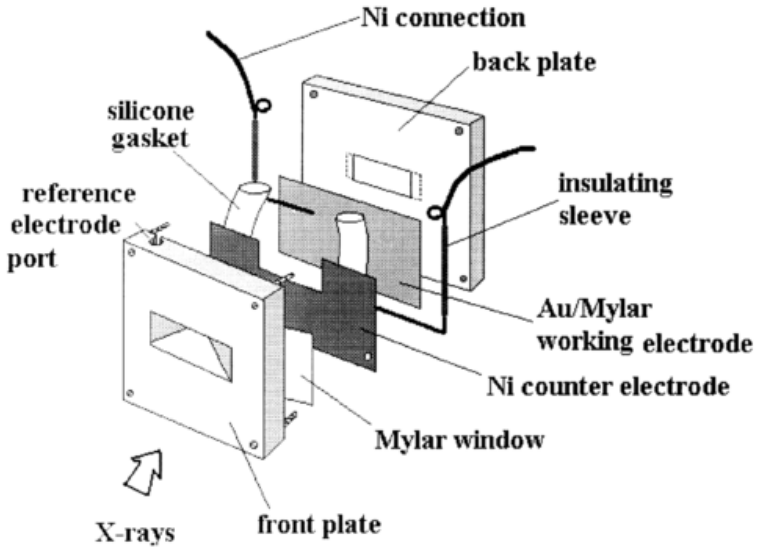

Figure 1.20 - Design of a hard X-ray *in situ* electrochemical cell.[63]

Although the sample cell in figure 1.21 is not designed for in situ electrochemical studies, it is a robust design suitable for XAFS and XRD measurements. This is useful as the improved functionality of the cell means more information about a material can be collected during the valuable beam time at a synchrotron facility. The use of many screws around the perimeter of the cell spreads the compressive pressure holding it together reducing the chances of leaks during experimentation.

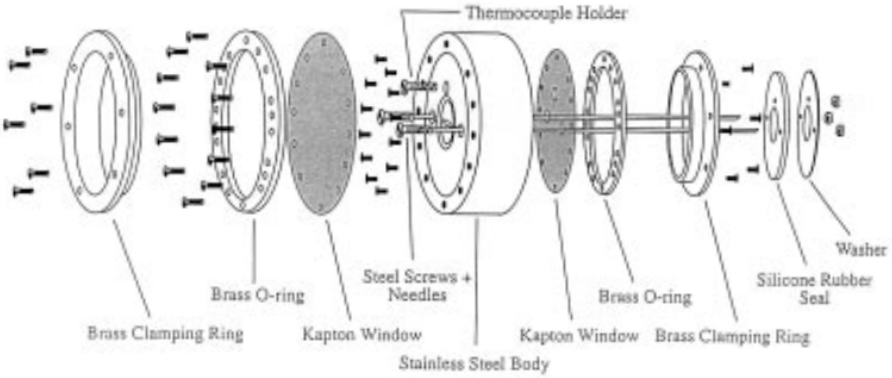

Figure 1.21 - Design of an electrochemical cell able to measure EXAFS and XRD.[64]

The cell in figure 1.22 is simple and designed specifically to measure thin films, if the working electrode was to be replaced with a TCO it could be possible to conduct *in situ* electrochemical studies also. It has an inlet and outlet for the electrolyte to be filled and drained and a luggin capillary to ensure that the reference electrode experiences an environment close to that of the working electrode. However it could be possible to improve the cell by reducing the size of the working electrode in comparison to the counter electrode.

Key

a) electrode holder
b) graphite sheet electrodes
c) rubber gasket
d) cell body and solution compartr
e) moving part
f) gold counter electrode
g) solution outlet
h) luggin capillary
i) solution inlet
j) X-ray window
k) electrical lead to counter electrode

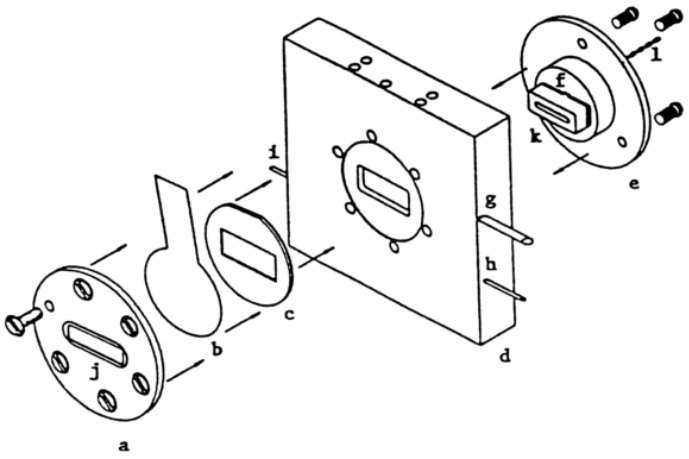

Figure 1.22 - Spectroelectrochemical cell designed to study thin films.[65]

The in situ cell in figure 1.23 has an inert Teflon body which can be used to measure XAFS of electrochemically active materials in transmission mode, however its design makes it difficult to flow or even replace the electrolyte. The working electrode surface area is also very large in comparison to the platinum counter electrode. The reference electrode is positioned quite far from the centre of the working electrode which is where the actual XAFS measurement would take place. The cell also only has 3 screws holding it together. If the pressure is not uniform across the 3 screws in the cell then leaks can occur. With no O-ring present at the front window it could be possible for leakage to occur from the front. However the design does mean that the path length of the electrolyte is reduced and reduces the X-ray attenuation from the electrolyte in transmission mode, giving an improved signal.

Key

1. Teflon cell body
2. Teflon cell body
3. Reference electrode
4. Pt counter electrode
5. Groove for counter electrode
6. Hole for reference electrode and electrolyte injection
7. O-ring
8. Carbon sheet working electrode
9. Filter paper with kapton tape
10. X-ray beam path
11. Screw hole
12. Screw

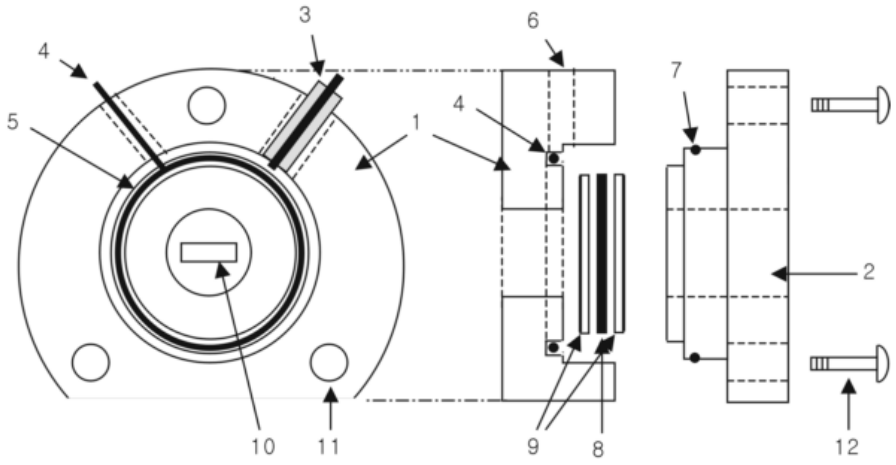

Figure 1.23 - Design for an electrochemical cell able to measure in transmission mode.[66]

1.9 Conclusion

This literature review covers several topics including the several polymorphs of nickel hydroxide and oxyhydroxide, various ways to synthesise the different forms of nickel hydroxide, and the effect of doping bulk powders and films with various elements. The effect of doping nickel hydroxide with metal ions affects the properties of the materials in several ways; addition of cobalt creates a highly electrically conductive Co^{3+} matrix within the nickel electrode and can increase the distance of the oxidation peak and the OER.

Addition of cadmium and zinc to the nickel hydroxide system stabilises the β-$Ni(OH)_2$ phase and have also been shown to increase the difference in electrical potential of the oxidation potential of the electrode and the OER, improving electrode durability.

Doping nickel hydroxide materials with manganese suggests that the trivalent state is most prevalent initially but converts to the tetravalent state on ageing in an alkaline solution. At 10 mole % manganese addition, it was found to substitute onto the nickel sites only and had little effect stabilising the α phase, however addition levels between 20-40%, found the manganese ions was also be present between the interlayers, thus stabilising the α-$Ni(OH)_2$ phase.

Additions of iron (III) ions stabilises the α-$Ni(OH)_2$ phase, however in thin films and electrodes it has shown to dramatically promote the OER of the electrolyte, making it very unsuitable for electrochromic materials but a good candidate for water splitting catalysis.

Additions of aluminium ions to nickel hydroxide materials also stabilised the α/γ redox couple, however aluminium cations at the interlayer have shown to be mobile during the charging and discharging cycle, leading to a loss of stability.

Basic electrochromic theory has been discussed as well as the components that make up spectroelectrochemical cells, which can be used to carry out *in situ* X-ray characterisation of different electroactive materials, therefore monitoring structural changes as a function of colour changes during a redox reaction. Various examples of *in situ* electrochemical cell designs were discussed and certain design features highlighted.

Chapter 2

Experimental

2.1 Introduction

As described previously the cathodic deposition and electrochemical cycling of nickel hydroxide is complex. The amorphous nature of the α-$Ni(OH)_2$ polymorph makes structural analysis of thin films and bulk powders difficult using in-house powder X-ray diffraction techniques. The use of synchrotron facilities such as the Diamond Light Source make it possible to study these materials using intense X-ray sources. Techniques such as X-ray absorption near edge structure (XANES), extended X-ray absorption fine structure (EXAFS) and X-ray diffraction (XRD) are powerful tools which can be used to further understand the local and long range structure due to the several orders of magnitude increase in energy intensity, which is able to probe poorly ordered materials. Important information such as bond lengths and oxidation states can be obtained through these methods.

2.2 Aims and Objectives

As discussed in the literature review, several polymorphs of nickel hydroxide can exist which are dependent on the preparation conditions, the aim of this research is to exploit the electrochemical advantages of the α/γ redox couple in order to improve performance of electrochromic thin films. Stabilisation of the α-$Ni(OH)_2$ phase could benefit electrochromic devices through:

- A larger number of exchanged electrons per nickel atom during electrochemical cycling due to higher oxidations states in γ-$Ni(OH)_2$ leading to improved coloration efficiency.
- A reduction in interlayer mechanical strain from overcharging to reduce material swelling - improved durability of the electrochromic layer within a device.

- A higher proton diffusion coefficient due to interlayer solvent molecules and charge balancing species - faster devices response time.

The objective was to design and fabricate an electrochemical cell which can be used on the I18 microfocus beamline at DLS, comparative samples of nickel hydroxide polymorphs will be studied with the synchrotron source.

2.3 Methods

2.3.1Nickel hydroxide based powders

Reported here is the experimental procedure used to synthesise nickel hydroxide powders. This section outlines the chemicals used and the experimental parameters targeted.

The following chemicals in table 2.1 were dissolved in deionised water (Milli-Q® deionised water 18.2 MΩ cm), without prior recrystallisation.

Chemical name	Chemical formula	Purity	Company
Nickel nitrate hexahydrate	$Ni(NO_3)_2 \cdot 6H_2O$	≥ 99%	Acros Organics
Nickel sulfate hexahydrate	$NiSO_4 \cdot 6H_2O$	≥ 99%	Sigma
Potassium hydroxide	KOH	≥ 85%	Fisher
Sodium carbonate	Na_2CO_3	≥ 99%	Fisher

Table 2.1 – Chemicals used for precipitation of nickel hydroxide powders

Nickel hydroxide powders were created through the chemical precipitation method. A constant dropwise addition of an aqueous alkaline solution (KOH, Na_2CO_3, 0.3 M, 0.6 M) was made to a magnetically stirred solution of an aqueous nickel hexahydrate salt solution ($Ni(NO_3)_2 \cdot 6H_2O$, $NiSO_4 \cdot 6H_2O$ 0.2 M) at room temperature. The solutions were stirred for a further 10 minutes to ensure a homogenous mixture. The resulting

light green precipitate was distributed evenly into four Nalgene HDPE bottles and stored at ambient room temperature (23 - 27°C) or in an oven (Carbolite PF60) at 85°C for either 1 day or 1 week.

Once the samples were aged for the desired amount of time, the liquid was decanted and the solid transferred to centrifuge tubes and filled with deionised water and spun for 10 minutes at 4000 rpm. The resulting green gel was washed under vacuum three times with deionised water (500 ml) to remove unwanted salts. The resulting gel was dried under vacuum to form a powder which was transferred to a ceramic crucible and dried overnight to constant weight at 50°C - 60°C.

For X-ray absorption measurements, 3 - 5 mg of nickel hydroxide powder was ground with ~50 mg of cellulose powder in an agate pestle and mortar, the resulting mixture was then hydraulically pressed in a 5 mm die at 10 tonnes for 5 minutes to form a pellet.

2.3.2 Nickel hydroxide thin films

The reproducible deposition of nickel hydroxide can be formed through a method similar to that of Carpenter et al[27]. Thin films were grown with a chronopotentiometry technique; a voltage is applied to maintain a constant current density to the working electrode in solution as a function of time (seconds). Depositions were made using 0.01 M $Ni(NO_3)_2$ solution. After deposition the working electrode was rinsed with deionised water and dried under a stream of nitrogen gas. A proposed reaction for the deposition of nickel hydroxide takes two steps as described below[67]. As the current density of 0.1 mA cm^{-2} is applied to the working electrode the negative potential increases rapidly to about - 0.9 V, as the film grows the potential decreases to maintain the constant current, the chemical equations are shown below.

$$NO_3^-{}_{(aq.)} + 7H_2O_{(l)} + 8e^- \rightarrow NH_4^+{}_{(aq.)} + 10OH^-{}_{(aq.)} \quad \text{Equation 2.1}$$

$$2OH^-{}_{(aq.)} + Ni^{2+}{}_{(aq.)} \rightarrow Ni(OH)_{2\,(s)} \quad \text{Equation 2.2}$$

Electrochemical cycling of the film was achieved by transferring the nickel hydroxide working electrode to a potassium hydroxide (0.1 M) electrolyte with a counter electrode, reference electrode and connecting to a potentiostat. Cyclic voltammetry was used to colour cycle, or a potential was set to colourise / bleach the film. Equation 2.3 describes chemically electrochromic colour cycling of the thin film material.

(Transparent green) $Ni(OH)_{2\ (s)} \leftrightarrow$ (Dark brown) $NiOOH_{(s)} + H^+{}_{(aq.)} + e^-$ Equation 2.3

2.3.4 Novel *in situ* electrochemical flow cell

For the *in situ* XAFS analysis of nickel hydroxide thin films, a nickel hydroxide thin film was electrochemically precipitated on an 1 cm^2 exposed piece of ITO polyester film for 600 seconds at a charge density of 0.1 mA cm^{-2} in a nitrogen purged aqueous solution of nickel nitrate (0.01 M).

To measure the change in the XANES of the nickel hydroxide thin film, the cell was drained of nickel nitrate and flushed with deionised water for 20 minutes. Nitrogen purged potassium hydroxide (0.1M) was pumped through the cell and a continuous potential was applied for 10 minutes before and during XANES measurements which were taken at 0.0 V, 0.4 V, 0.5 V, 0.6 V (Vs. Ag/AgCl).

2.4 Characterisation methods

The selected characterisation techniques used in the experiments are summarised below, with specifics on how they were applied to carry out the identification of nickel hydroxide powders and thin films.

2.4.1 ATR - FTIR

FTIR spectroscopy is a powerful and well established characterisation technique which measures the infrared light absorbed by a sample at a range of given frequencies. As described in the previous literature, it can quickly determine the phase of nickel hydroxide present through the presence or lack of hydrogen bonding peaks in the spectra. Table 2.2 shows phase identifying bands present in nickel hydroxide materials.

Phase	**Band position**
β-$Ni(OH)_2$	OH 3650 cm^{-1} narrow, non hydrogen bonded ^{-}OH
α-$Ni(OH)_2$	Around OH 3500 cm^{-1} Asymmetric broad

Table 2.2 – Characteristic band positions in FTIR of β-$Ni(OH)_2$ and α-$Ni(OH)_2$

With the addition of an attenuated total reflection (ATR) attachment, sample preparation is simple, powdered sample is placed against the instruments crystal with a high refraction index. Infrared light is passed through the crystal and penetrates into the sample by a few microns which is reflected back into the instrument.

FTIR data were collected on a Perkin Elmer Spectrum 100 FTIR spectrophotometer fitted with an attenuated total reflection unit. The sample stage was cleaned with methanol and the background signal recorded before measurements were taken. The samples were analysed between 4000 – 500 cm^{-1}.

2.4.2 XRD

Powder X-ray Diffraction (XRD) is commonly used to identify crystalline phases of powdered materials. Bragg's law (Equation 2.4) defines this phenomenon where n is a positive integer, λ is the wavelength of the X-ray, d is the interplanar distance and θ is the scatter angle.

$$n\lambda=2d\sin\theta \qquad \text{Equation 2.4}$$

Intensities at different angles can be simply compared to reference data or cards in a database, or crystal parameters can be calculated through cell refinement. As described previously, nickel hydroxide phases can be easily identified through its characteristic (001) peak as shown in table 2.3.

D-Spacing	2Theta CuK	Reflection intensity	(*h,k,l*)
4.60	19.26	100.00	(0,0,1)
2.71	33.07	45.00	(1,0,0)
2.33	38.54	100.00	(1,0,1)

Table 2.3 – 3 most intense PXRD peak positions β-Ni(OH)$_2$ ICCD card 14-117

Also as mentioned in the literature review, peak broadening is a result of reduced crystallinity and selective peak broadening indicated reduction in order along certain axis such as the turbostratic nature of α-Ni(OH)$_2$ in the c direction.

For X-ray diffraction measurements, a Bruker D2 Phaser Cu K_α, and a Bruker D8 Advance Cu $K_{\alpha1}$ were used with a 2θ range of 5 - 65°. For sample preparation, approximately 0.2 g of nickel hydroxide was ground to a fine powder in an agate pestle and mortar, a few drops of acetone were added and mixed to form a slurry which was then applied to a silicon wafer XRD sample holder.

2.5 Generation of Synchrotron Radiation

Synchrotron radiation sources, known as "synchrotrons" are research facilities used to produce intense beams of light. The radiation was originally considered an inefficiency of early high energy physics research, now synchrotron facilities are designed to produce stable and powerful sources of electromagnetic radiation. Figure 2.1 shows a schematic of the Diamond Light Source Synchrotron facility.

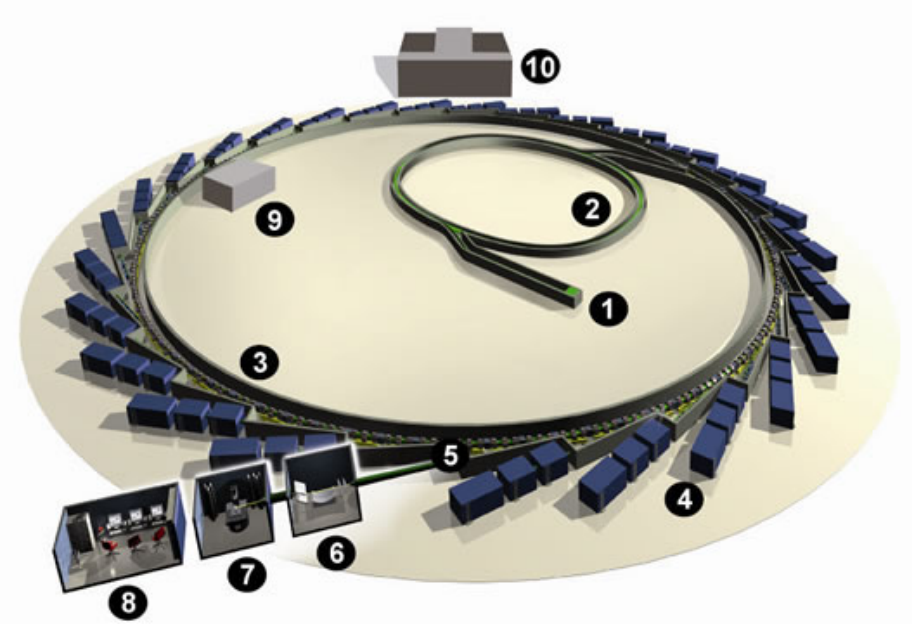

Figure 2.1 - Diagram of the Diamond Light Source synchrotron facility. (1) Injection system and Linac (2) Booster Synchrotron (3) Storage ring (4) Beamline (5) Front end (6) Optics hutch (7) Experimental hutch (8) Control Cabin (9) RF cavity (10) Diamond house.[68]

Electrons are fired from an electron gun in an evacuated tube where they pass into a linear accelerator. The electrons are then passed into the booster ring where the packets of electrons are accelerated to near the speed of light. These packets of electrons are injected into the storage ring, when the electrons travelling at relativistic speeds are forced to change direction via bending magnets. As they do so

they emit intense directional x-rays which can be used for scientific experiments. Insertion devices such as "wigglers" and "undulates" are used in increase the intensity or change a characteristic of the light generated by passing the electrons through arrays of powerful alternating magnets. The electrons speeds within the storage ring are maintained by the RF cavities and the emitted X-ray light is passed through to the beamline. Experiments are performed under remote control through the control cabin as the radiation exposure within the optical and experimental cabin would harm individuals inside. Large amounts of electromagnetic shielding is found around the synchrotron and in each of the beam lines to protect the users and workers.

2.5.1 XAFS

X-ray Absorption Fine Structure (XAFS) which falls under the umbrella of X-ray absorption spectroscopy (XAS) techniques, XAFS is a powerful and versatile technique for characterising the local structure of materials and used in a wide range of scientific disciplines. Due to the requirement for a tuneable X-ray source, XAFS experiments are currently only conducted at synchrotron facilities.[69]

The principle behind XAFS is that X-ray absorption coefficient μ(E), which is how strongly X-rays are absorbed by a material as a function of X-ray energy, is absorbed less as the energy increases due to the X-ray becoming more penetrating. However characteristic to each element, a sudden increase in X-ray absorption can be observed at specific X-ray energies; this is known as the absorption edge. This is due to there being enough energy to liberate an electron from a low lying orbital (such as 1s) to generate a photoelectron. This short lived photoelectron scatters to neighbouring atoms, the interference caused of this can be observed through the fluctuation of the X-ray absorption coefficient, the change in shape and position of

the edge spectrum. The resulting phenomenon resulting from an XAFS experiment can be split into two sections; the X-ray Absorption Near Edge Structure (XANES) region and the Extended X-ray Absorption Fine Structure (EXAFS) region as shown In figure 2.2.

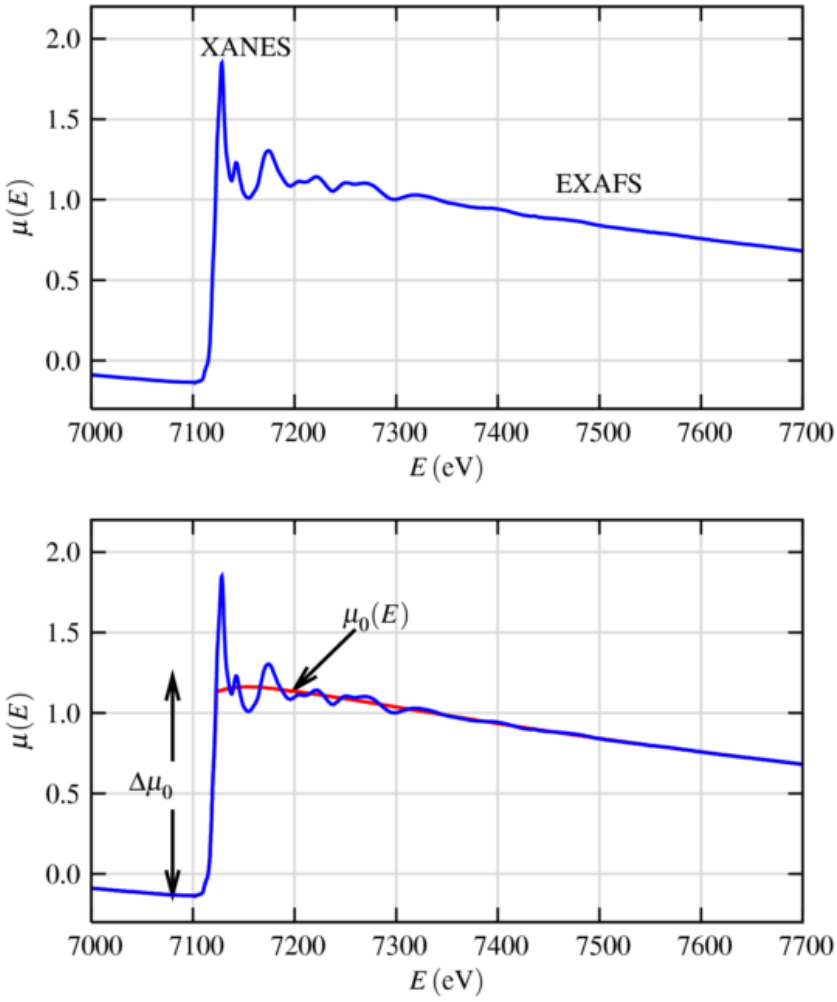

Figure 2.2 - XAFS μ(E) for FeO (top) measured XAFS spectrum showing XANES and EXAFS regions, (bottom) μ(E) is shown with smooth background function $\mu_0(E)$.[70]

The XANES region (also referred as Near Edge X-ray Absorption Fine Structure, NEXAFS) only looks at the area before and just after the edge. It includes any pre-

edge features and typically continues on to 50 - 100 eV above the edge step. Currently there is no underlying equation quantifying the XANES region, however XANES analysis is sensitive to formal valance, coordination environment, and ligand type. Model compounds can be used to compare against the material under investigation and general observations of the absorption peak shift can be made.

The EXAFS region however requires manipulation of the signal to obtain any useful information as shown by the steps below.[70]

- Convert measured intensities to μ(*E*), correcting for experiment related errors such as self-absorption and detector dead time.
- Subtract a smooth pre-edge function from μ(*E*) to get rid of any instrumental background and absorption from other edges.
- Identify the threshold energy, E_0, usually as the energy of the maximum derivative of μ(*E*).
- Normalise μ(*E*) to go from 0 to 1, so that it represents the absorption of 1 x-ray. This normalised spectra is useful for XANES analysis.
- Remove the smooth post-edge background function to approximate $\mu_0(E)$.
- Isolate the XAFS $\chi(k)$, where $k = \sqrt{2m(E - E_0/\hbar^2}$
- *k*-weight the XAFS $\chi(k)$ and Fourier transform into R-space.

Once the data have been processed, the signal can be refined against a model which can confirm the position and bond distances of nearby atoms. The EXAFS equation (equation 2.5) is used in order to calculate the resulting signal from the scattering of neighbouring atoms where, $f(k)$ and $\delta(k)$ are scattering properties of nearby atoms, N is the number of nearby atoms, R is the distance of these atoms from the absorbing atom and σ^2 is the disorder of the distance.

$$\chi(k) = \sum_j \frac{N_j f_j(k) e^{-2k^2\sigma_j^2}}{kR_j^2} \sin[2kR_j + \delta_j(k)] \qquad \text{Equation 2.5}$$

From this, if the scattering amplitude $f(k)$ and scattering phase shift $\delta(k)$ are known both the position and atomic species in the surrounding shells of the absorbing atom can be calculated.[69,70]

Chapter 3

Characterisation of Nickel Hydroxide Materials

3.1 Results and discussion

This section summarises the results from the characterisation of nickel hydroxide powders synthesised via the chemical precipitation method as described in chapter 3. The results are focused into two groups; 1. nickel hydroxides precipitates prepared from a nickel nitrate precursor solution and 2. nickel hydroxides precipitates prepared from a nickel sulfate precursor solution. The phases are characterised using PXRD and FTIR, samples were further characterised by EXAFS. Many more powders were synthesised, however the following powders were selected for their distinct phase purity. The reason for the synthesis and characterisation of the powders is to use them as standards so that phases present in nickel hydroxide thin films deposited in the novel *in situ* electrochemical cell, can be identified via XAFS and XRD.

3.1.1 Nickel hydroxide powders

The experimental conditions used to prepare the set of samples for analysis are given in table 3.1 and 3.2, along with the crystalline phase identified from analysis of PXRD and FTIR data. “RT” is used to denote room temperature as the temperature was not externally controlled and ranged between 23-27°C.

Nickel salt	Base	Temperature	Duration	Majority Phase
$Ni(NO_3)_2$ 0.2 M	KOH 0.3 M	85°C	1 Week	β-$Ni(OH)_2$
$Ni(NO_3)_2$ 0.2 M	KOH 0.3 M	RT	1 Day	β*-$Ni(OH)_2$
$Ni(NO_3)_2$ 0.2 M	KOH 0.6 M	RT	1 Week	β_{BC}-$Ni(OH)_2$
$Ni(NO_3)_2$ 0.2 M	Na_2CO_3 0.6 M	RT	1 Week	α-$Ni(OH)_2$
$Ni(NO_3)_2$ 0.2 M	Na_2CO_3 0.6 M	85°C	1 Week	β*-$Ni(OH)_2$

Table 3.1 Synthesis conditions used and phases identified of PXRD of using nickel nitrate precursor

Nickel salt	Base	Temperature	Duration	Phase
$NiSO_4$ 0.2 M	KOH 0.3 M	RT	1 Day	α-$Ni(OH)_2$
$NiSO_4$ 0.2 M	KOH 0.3 M	85°C	1 Week	β-$Ni(OH)_2$
$NiSO_4$ 0.2 M	KOH 0.6 M	RT	1 Week	β_{BC}-$Ni(OH)_2$
$NiSO_4$ 0.2 M	Na_2CO_3 0.6 M	RT	1 Week	α-$Ni(OH)_2$
$NiSO_4$ 0.2 M	Na_2CO_3 0.6 M	85°C	1 Week	β*-$Ni(OH)_2$

Table 3.2 Synthesis conditions used and phases identified of PXRD of using nickel sulfate precursor

Shown in figure 3.1, nickel precursors reacted with potassium hydroxide (0.3 M) and stored at an elevated temperature (85°C) show a high level of crystallinity in the powder XRD patterns and an intense (001) peak around 19° 2θ. In addition, the FTIR shows a sharp absorption band around 3650 cm^{-1} in figure 3.2 which indicates that no hydrogen bonding from molecular water is present between the nickel

hydroxide layers. As supported by the literature, reacting the material in an alkaline environment for extended periods of time forms the β-$Ni(OH)_2$ phase.

Nickel nitrate (200 ml, 0.2 M) and nickel sulfate (200 ml, 0.2 M) solutions reacted with sodium carbonate (200 ml, 0.6 M) at room temperature for one week and nickel sulfate precursor reacted with potassium hydroxide (0.3 M) for 24 hours at ambient temperatures form light green crystals of nickel hydroxide. As shown in figure 3.3, samples are amorphous in PXRD and all show broad bands in the FTIR (figure 3.4) around 3400 cm^{-1}. They are similar but not identical, this still suggests that the phase is α-$Ni(OH)_2$ due to the presence of hydrogen bonded water molecules between the turbrostratic sheets of nickel hydroxide in the FTIR spectra.

But in comparison to nickel nitrate reacted with potassium hydroxide (0.3 M) at room temperature for 24 hours, the sample shows some level of crystallinity in the XRD (figure 3.5) around 15° 2θ and both a sharp band at 3650 cm^{-1} and a broad band at 3400 cm^{-1} (figure 3.6) suggesting a phase known in the literature as β*-$Ni(OH)_2$.

Synthesised samples from both nickel nitrate and nickel sulfate solutions with sodium carbonate (0.6 M) at elevated temperatures (85°C) present a phase with similar characteristics.

Finally samples precipitated from nickel nitrate and nickel sulfate with potassium hydroxide (0.6 M) for 1 week at ambient temperatures show peaks in the XRD (figure 3.7) around 19° 2θ but are very broad suggesting that the samples are not very crystalline, however the FTIR (figure 3.8) show strong shape absorption peaks around 3650cm^{-1}, the sample prepared with the sulfate precursor shows some level of molecular water present in the layers by a small broad band around 3400 cm^{-1}. These samples have been denoted in the literature as badly crystalline beta nickel hydroxide or β_{BC}-$Ni(OH)_2$.

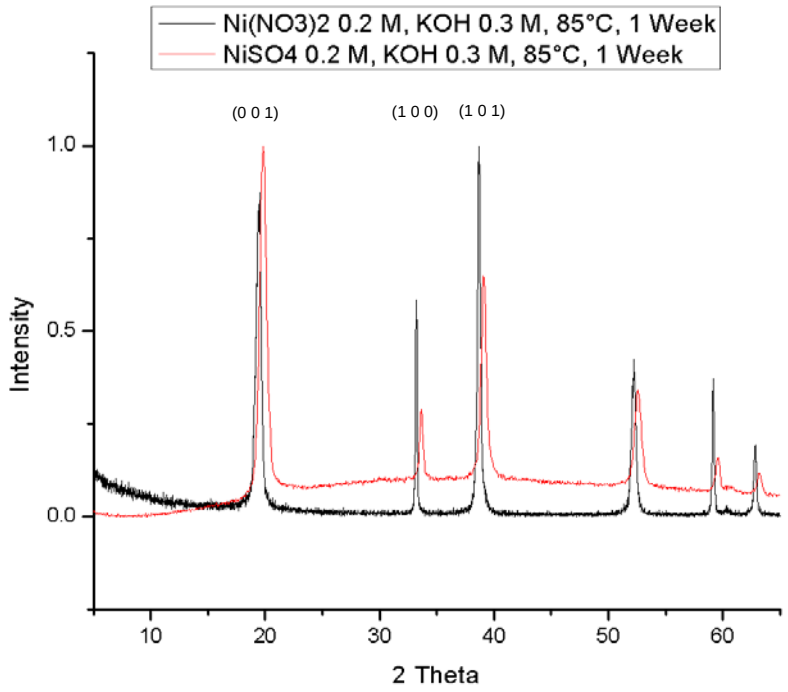

PDF number 14 -117 theophrastite, 3 most intense peaks		
d- space	**2 Theta**	***h, k ,l***
4.60	19.26	(0 0 1)
2.70	33.07	(1 0 0)
2.33	38.54	(1 0 1)

Figure 3.1 – PXRD data of β-Ni(OH)$_2$ phases

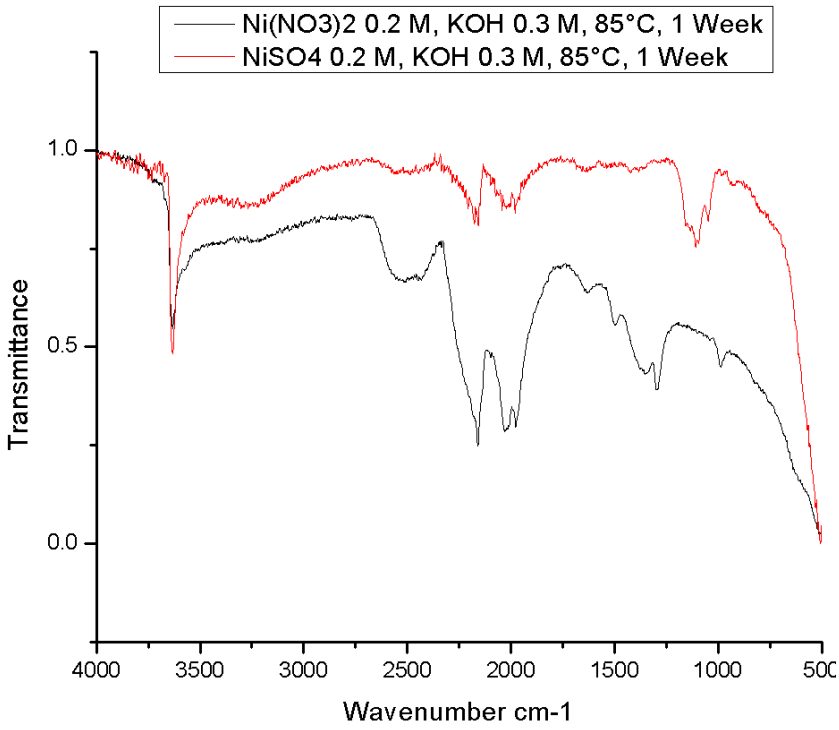

Figure 3.2 – FTIR data of β-Ni(OH)$_2$ phases

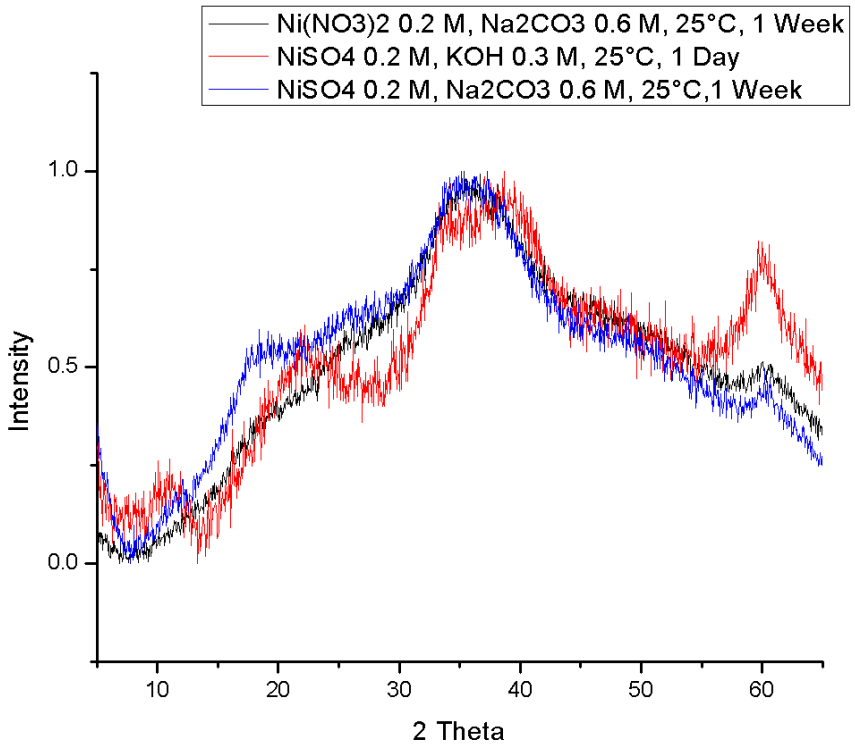

Figure 3.3 – PXRD data of amorphous phases likely to be α-Ni(OH)$_2$

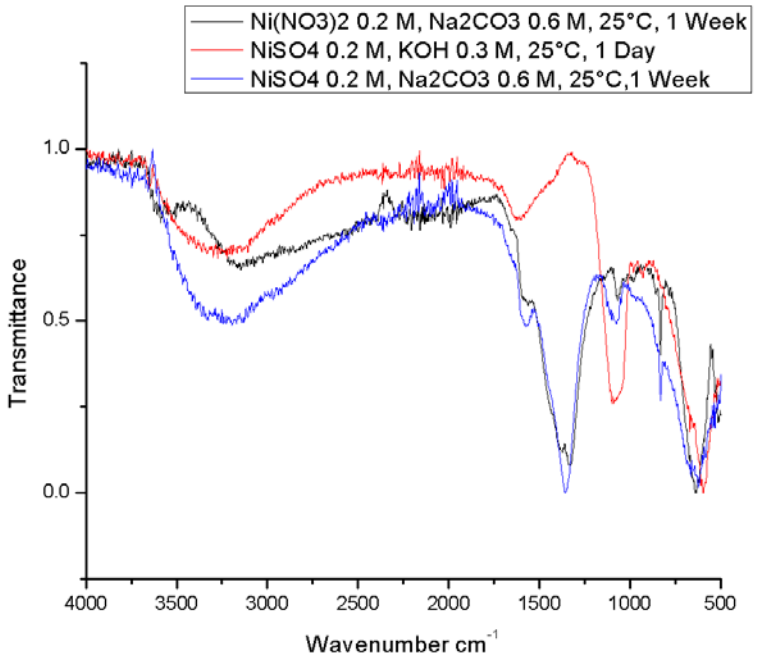

Figure 3.4 – FTIR spectra of amorphous α-Ni(OH)$_2$ samples

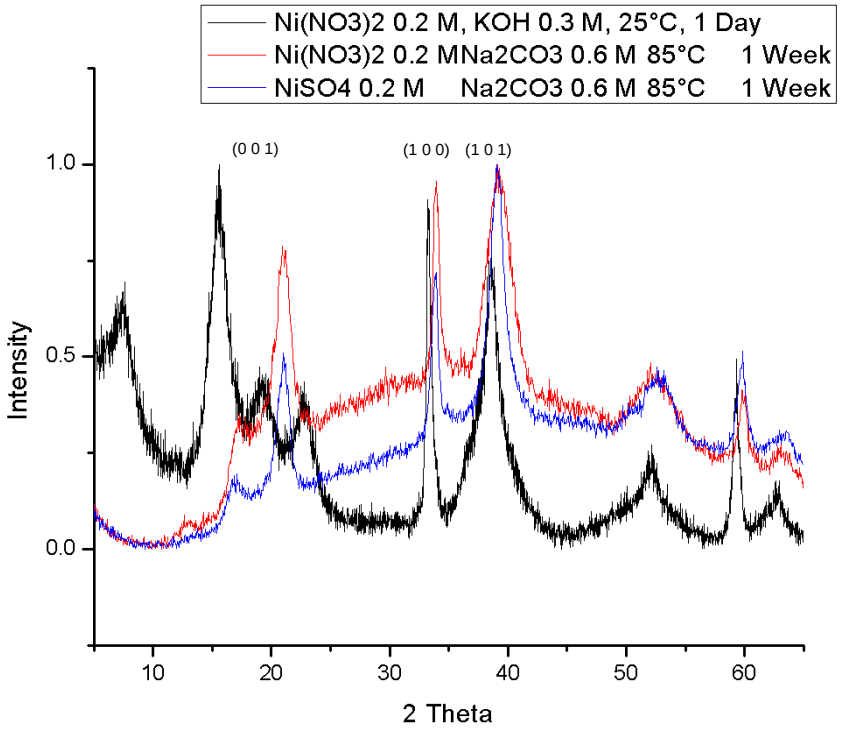

PDF number 14 -117 theophrastite, 3 most intense peaks		
d- space	**2 Theta**	***h, k ,l***
4.60	19.26	(0 0 1)
2.70	33.07	(1 0 0)
2.33	38.54	(1 0 1)

Figure 3.5 – PXRD data of β*-Ni(OH)$_2$ phases

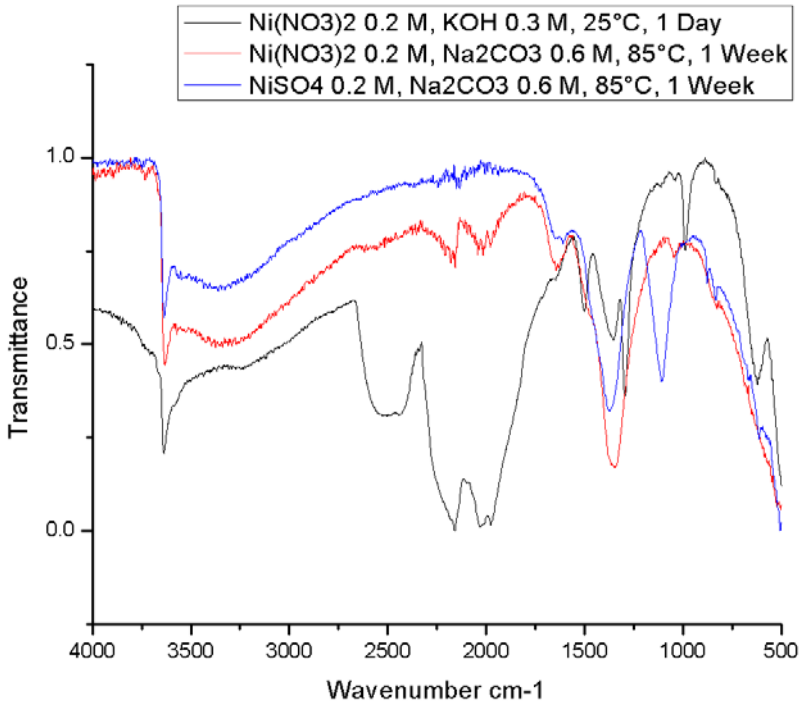

Figure 3.6 – FTIR data of β*-Ni(OH)$_2$ phases

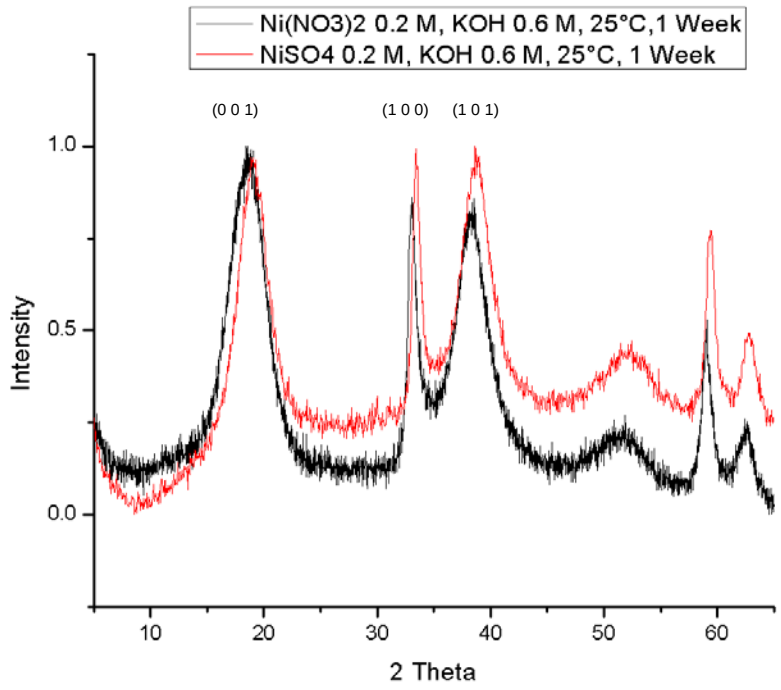

PDF number 14 -117 theophrastite, 3 most intense peaks		
d- space	**2 Theta**	***h, k ,l***
4.60	19.26	(0 0 1)
2.70	33.07	(1 0 0)
2.33	38.54	(1 0 1)

Figure 3.7 – PXRD of β_{BC}-$Ni(OH)_2$ phases

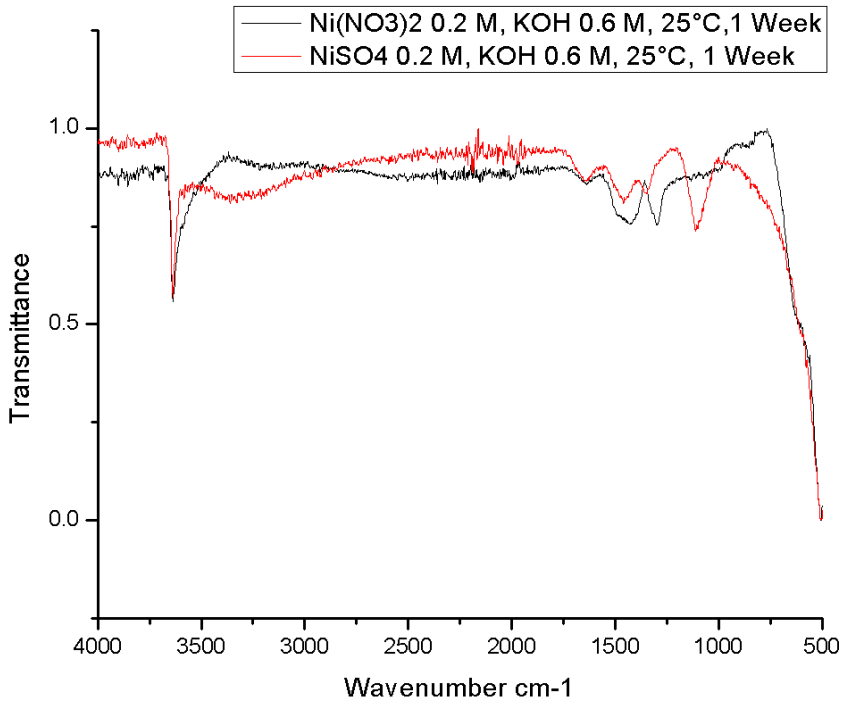

Figure 3.8 – FTIR spectra of β_{BC}-$Ni(OH)_2$ phases

3.1.2 XAFS studies

The set of samples discussed above were analysed using X-ray absorption fine structure spectroscopy, figures 3.9 – 3.12 show nickel hydroxide phases as described above in R space, a radial distribution of atomic shells from an absorbing nickel atom in Ångström.

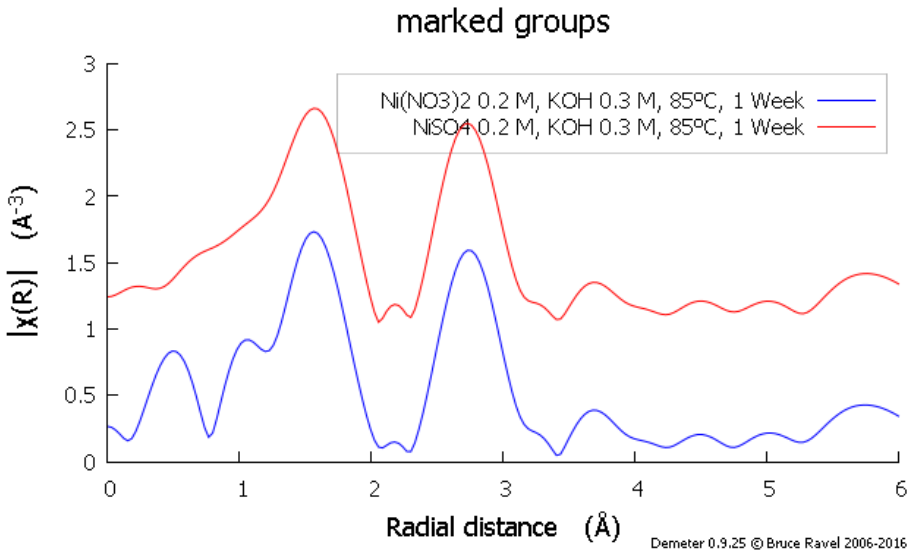

Figure 3.9 - XAFS data of β-Ni(OH)$_2$ samples in R space (top) nickel hydroxide synthesised nickel sulfate and potassium hydroxide at 85°C for 1 week (bottom) Nickel hydroxide synthesised from nickel nitrate and potassium hydroxide for 1 week.

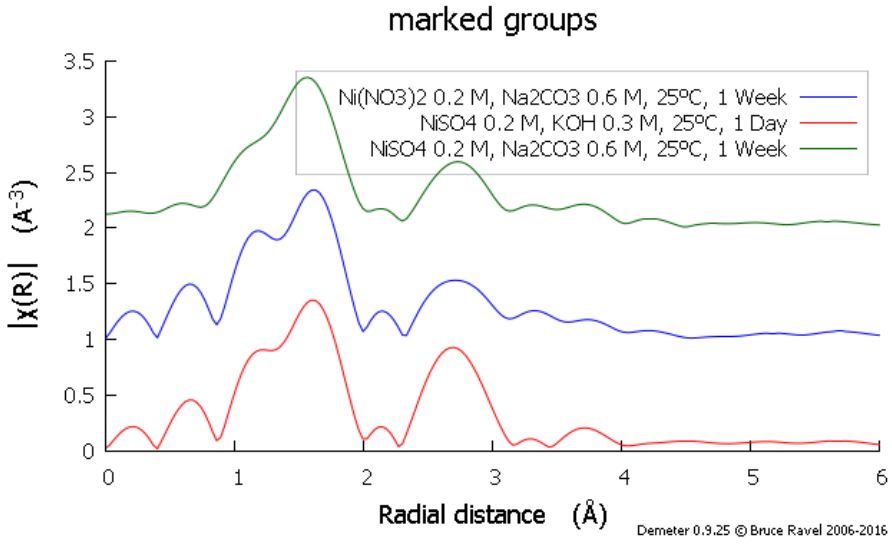

Figure 3.10 –XAFS data of α-Ni(OH)$_2$ samples in R space (top) Nickel hydroxide synthesised from nickel sulfate and sodium carbonate at room temperature for 1 week (middle) nickel hydroxide synthesised from nickel nitrate and sodium carbonate at room temperature for 1 week (bottom) nickel hydroxide synthesised from nickel sulfate an potassium hydroxide at room temperature for 1 day.

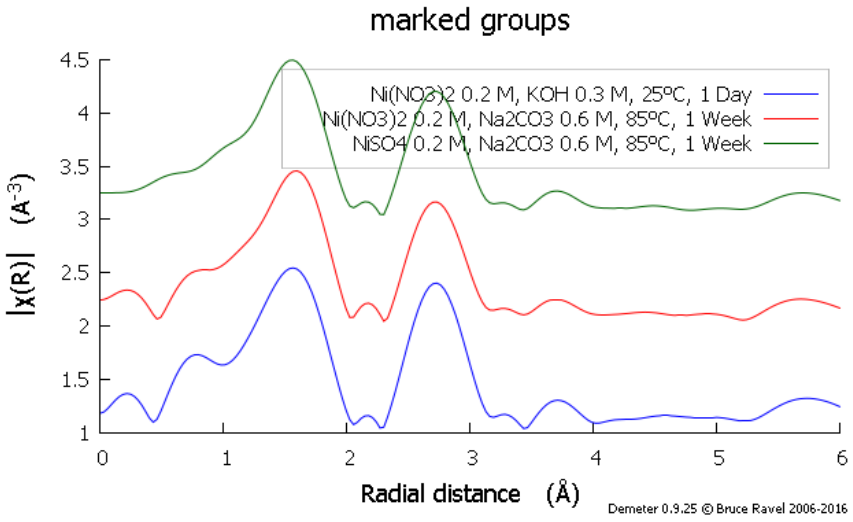

Figure 3.11 – XAFS data of β*-Ni(OH)$_2$ samples in R space (top) Nickel hydroxide synthesised from nickel sulfate and sodium carbonate at 85°C for 1 week (middle) nickel hydroxide synthesised from nickel nitrate and sodium carbonate at 85°C for 1 week (bottom) Nickel hydroxide synthesised from nickel nitrate and potassium hydroxide at room temperature for 1 day.

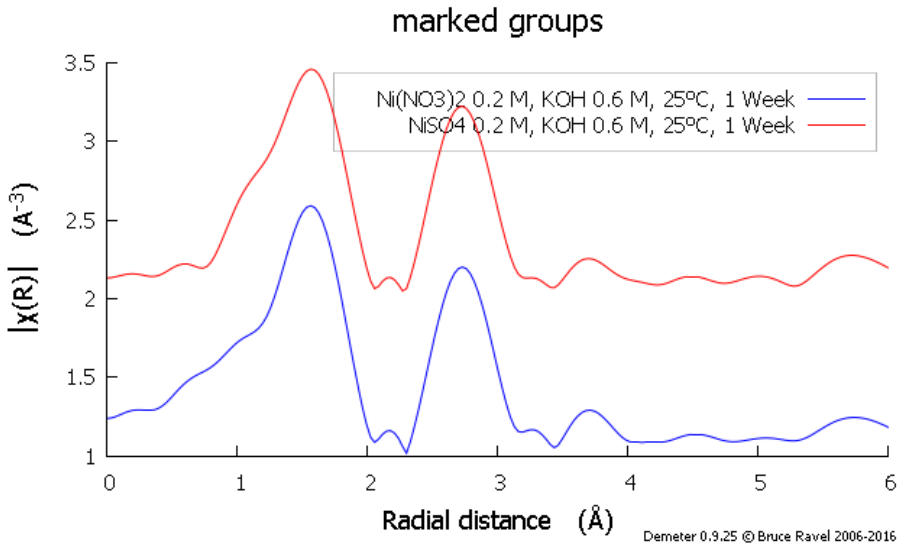

Figure 3.12 – XAFS data of β_{BC}-$Ni(OH)_2$ samples in R space (top) nickel hydroxide synthesised from nickel sulfate and potassium hydroxide at room temperature for 1 week (bottom) nickel hydroxide synthesised from nickel nitrate and potassium hydroxide at room temperature for 1 week.

To conclude this section we have shown that different crystallographic phases of nickel hydroxide can be synthesised simply by changing the experimental parameters of the precipitation reaction. Longer reaction times, higher pH and elevated temperatures lead to a more crystalline phase developing as in β-$Ni(OH)_2$. Milder reaction conditions lead to an amorphous phase with nickel hydroxide layers intercalated with water molecules and possible stabilising anions.

In addition, the phase highlighted in the literature called β*-$Ni(OH)_2$ has been identified which has a mixture of both α-$Ni(OH)_2$ and β-$Ni(OH)_2$ phase present, and the phase β_{BC}-$Ni(OH)_2$ which resamples a less crystalline version of β-$Ni(OH)_2$.

Chapter 4

Development of novel *in situ* electrochemical cell for use with advanced microfocus synchrotron techniques

4.1 Introduction

The greatest differences between a typical electrochemical cell and a spectroelectrochemical cell is the requirement for the cell to not only perform redox reactions, but also to allow external equipment to measure a property under potential control. This means there is a compromise between an ideal electrode geometry and the positioning of the material under investigation. A new cell design was required to characterise nickel hydroxide thin films on the I18 microfocus EXAFS beam line at the Diamond Light Source Synchrotron facility. The design required the ability to measure electrochromic thin films using UV-Vis in transmission to study the colour change of the films but also XAFS and microfocus X-ray fluorescence mapping (μXRF) of the thin film under potential control. The cell was also designed for XRD measurements of the thin film via transmission through the cell, however this was not achieved.

4.2 Novel *in situ* electrochemical flow cell for UV-Vis and microfocus XAFS/XRD

Reported here is the description and assembly of the cell (figure 4.1) and the peripheral systems. The cell required all of the critical components as mentioned in the previous literature review in chapter 2 and will refer to the schematic in figure 4.2.

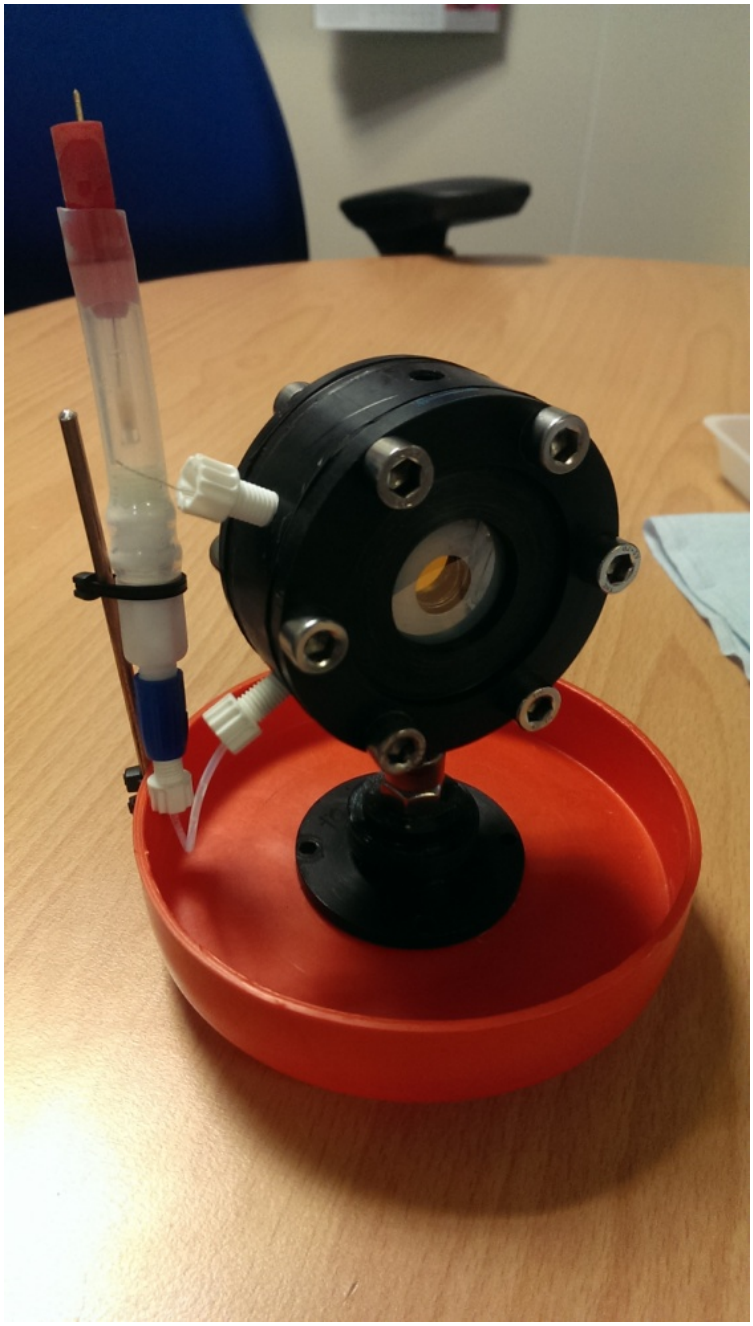

Figure 4.1 - Assembled *in situ* electrochemical cell

Part Key

A - Cell body

A^1 - Front cover

A^2 - Main Cell body

A^3 - Middle conical part

A^4 - Rear conical part

B - Platinum wire coil CE

C - Electrolyte outlet port

D - Gold wire WE connection

E - ITO polyester film WE / front window

F - Electrolyte inlet port

G - Mounting post

H - Luggin capillary to Ag/AgCl RE

I - Polypropylene insulating spacer

J - Kapton foil rear window

K - Screw holes

L - O - ring

M - Neoprene gasket

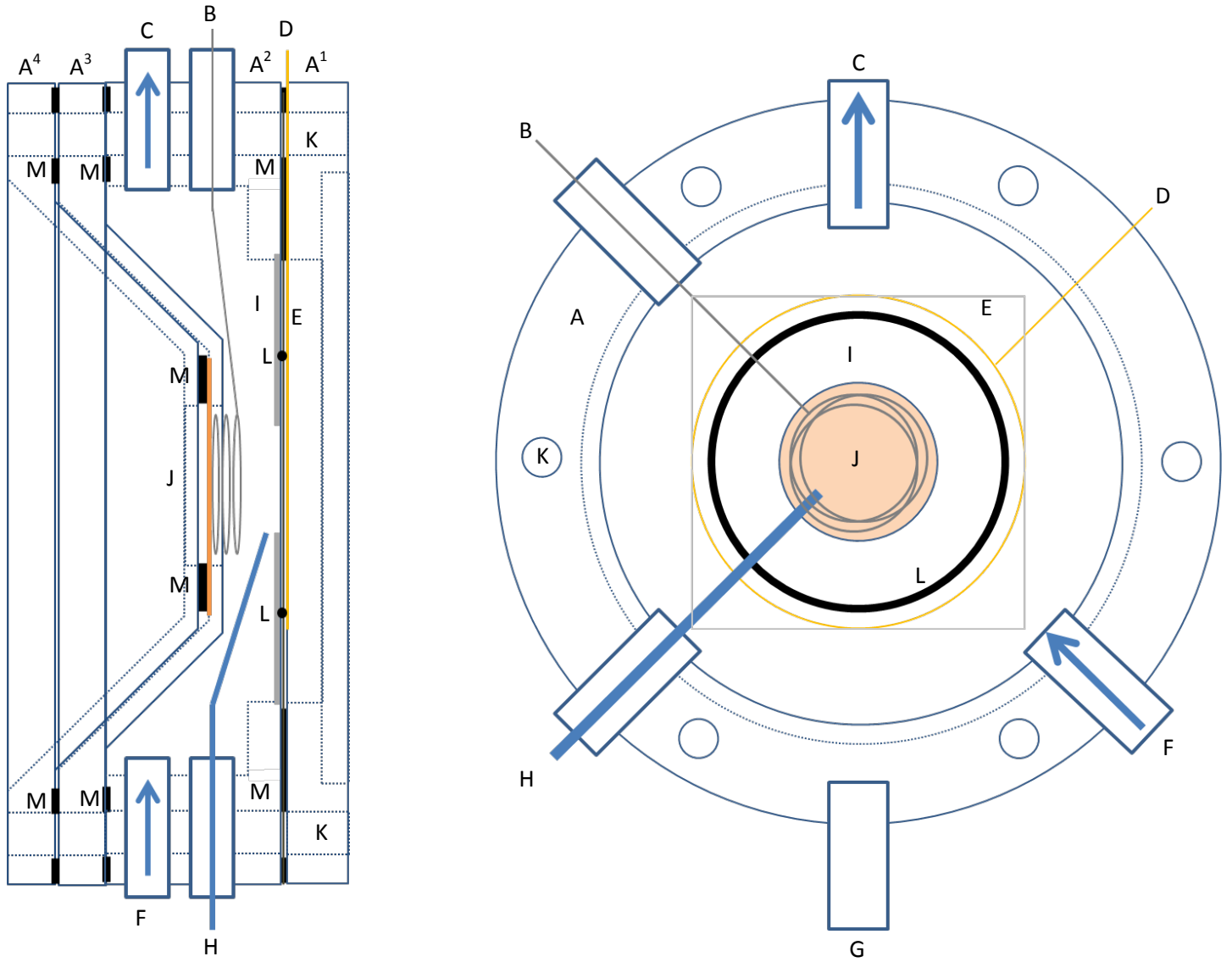

Figure 4.2 - Diagrams of *in situ* cell, (left) side profile, (right) front view

Reported here is the description and assembly of the cell and the peripheral systems. The cell required all of the critical components as mentioned in the previous literature review in chapter 2 and will refer to the schematic in figure 4.2.

The cell body (part A) was made from a nylon rod (RS components, 65 mm diameter) this was cut and machined on a lathe, the material was inexpensive, inert to the chemicals used in this experiment and easy to machine / thread holes. Neoprene sheets (RS components) were cut to form gaskets (part M) to prevent leakages of the cell and an O-ring (part L) was positioned to prevent leaks from the front window when the cell was sealed.

The working electrode was formed from an ITO coated polyester film (Visiontek Systems, 50 Ω per square) (part E) with a gold wire perimeter (part D) to improve conductivity and form a connection to the potentiostat. The polymer TCO's transparent nature allows UV-Vis measurements to observe the colouration cycles, in addition the beamline cameras could view the colour change to confirm the cell was working. The secondary benefit to having the ITO polyester material as the working electrode was that the material is strong but also thin. Thus it can be used as an X-ray window into the cell and grow films internally, reducing the attenuation of fluorescence signal from the nickel hydroxide material under study. A small polypropylene spacer (part I) was used to insulate and limit the exposed ITO surface to 1 cm^2 to grow the thin film. Kapton foil (part J) with a neoprene gasket (part M) was positioned at the back of the cell to act as a second window which was also transparent, thin and chemically inert.

The counter electrode was a platinum wire coil (Goodfellow 0.3 mm x 0.2 m) (part B), this prevented the electrode from obscuring light path from the UV-Vis

measurements or XRD measurements made in transmission. Due to limited space in the cell a luggin capillary from semi-ridged PTFE tubing (part H) was positioned between the working electrode and the counter electrode connected to a low profile Ag/AgCl (Pine Research, 3.5 mm) reference electrode held in a solution with a piece of tubing and tap to aid filling and draining of the luggin capillary. The cell was mounted on a holding post (part G) and positioned above a drip tray to protect equipment if a leakage occurred.

As mentioned previously, thin films of nickel hydroxide can be deposited in a dilute solution of nickel nitrate, however to observe the electrochromic properties, the electrolyte needs to be replaced with potassium hydroxide. Rather than disassembling the cell to change the electrolyte, the cell was designed to be filled, washed and drained using a peristaltic pump (Cole Parmer, Masterflex) and a series of threaded taps and tubes (Kinesis, Omnifit). This has several benefits; time saved during beamtime; nitrogen can also be continuously purged reducing the effect of the oxygen evolution reaction in addition to pushing any air bubbles through and out of the system; the flow of electrolyte reduces the effect of localised heating / boiling of the thin film during the use of intense X-ray energy. The following images demonstrate how the cell was assembled.

Figure 4.3 - (Left to right) rear conical part A4, middle conical part A3, main body A2, front cover A1

Figure 4.4 - Close up of the main body of cell showing luggin capillary part H and platinum coil counter electrode part B

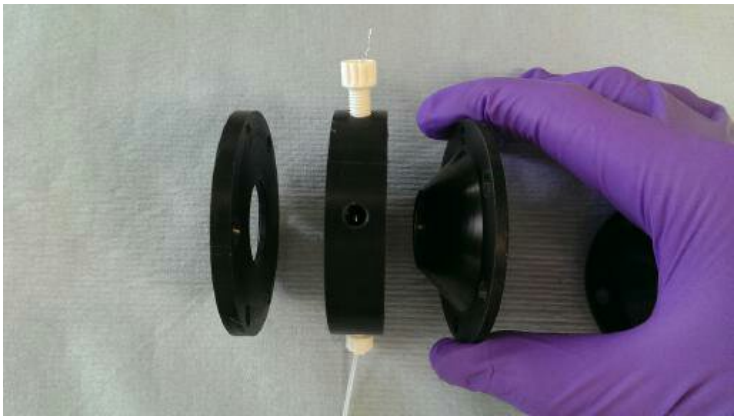

Figure 4.5 - Side profile showing front cover A1, main body A2 and middle conical part A3 / A4

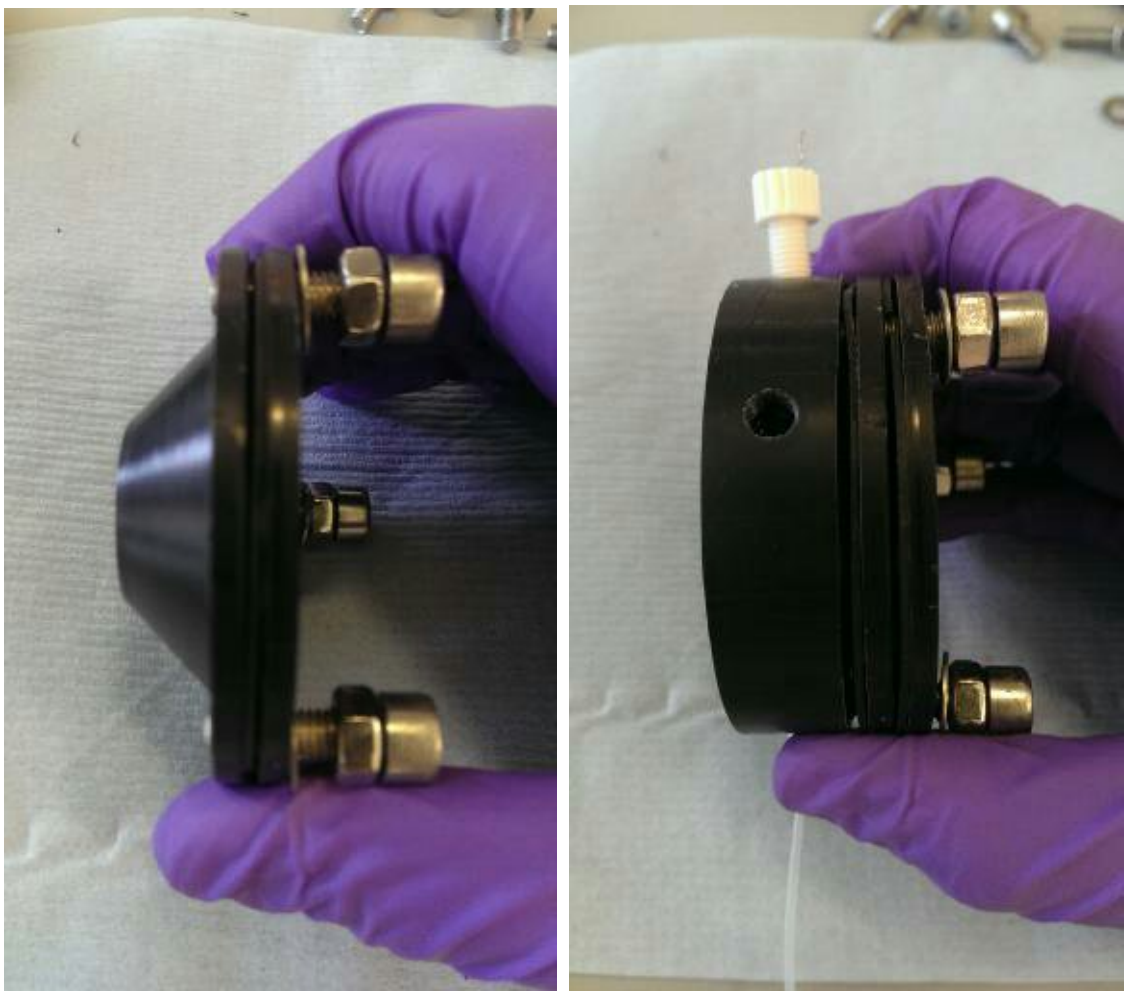

Figure 4.6 - (Left) rear A4 and middle A3 conical parts screwed together with kapton foil J and gasket M inside (not shown) (Right) insertion of rear window A3 / A4 assembly into main body of cell A2.

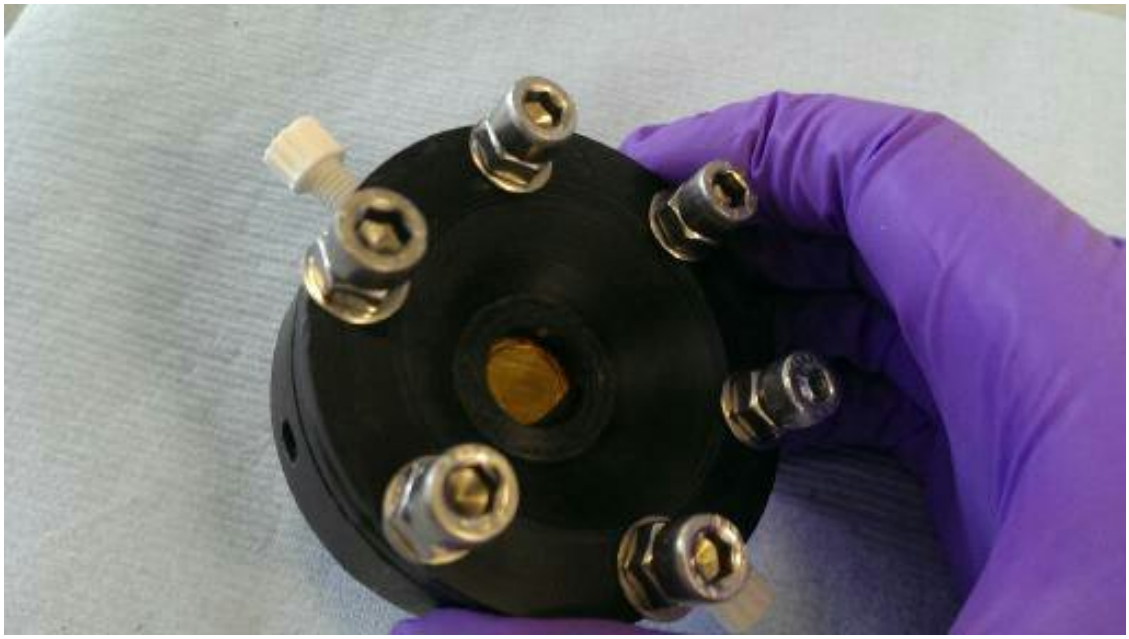

Figure 4.7 - Assembly of rear kapton window J remaining screws inserted

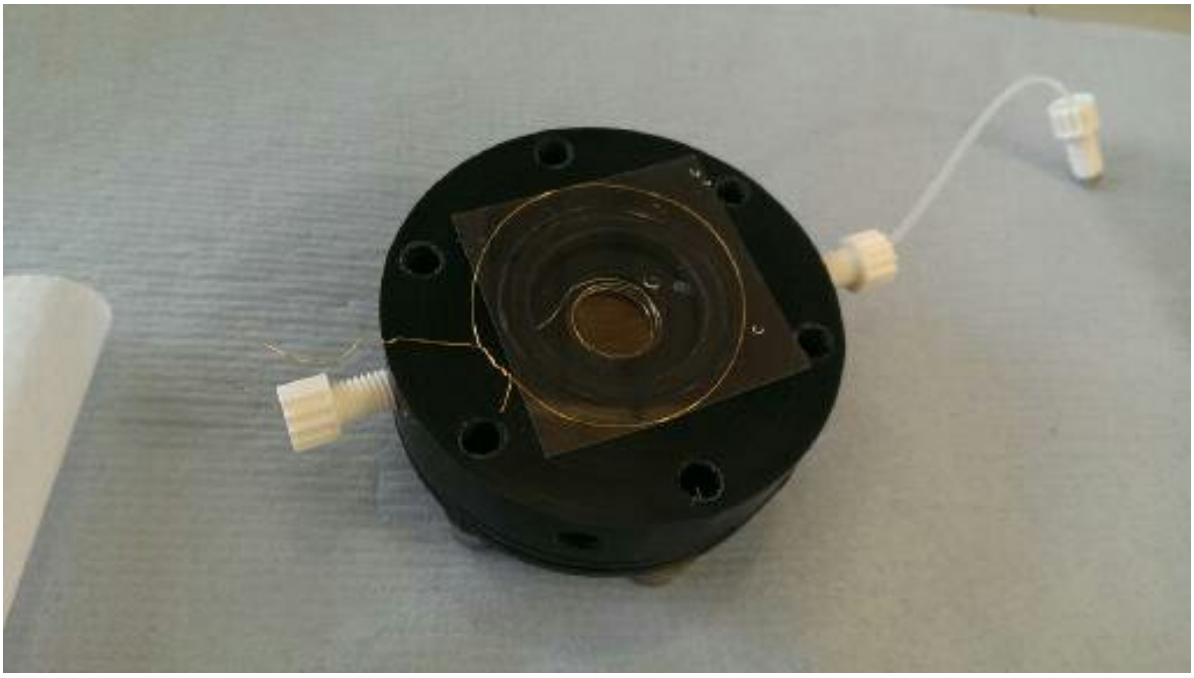

Figure 4.8 - Installation of front working electrode E, gold wire D placed between cell body A2 and ITO polyester film, gasket M and front cover A1 to be installed (not shown) O ring L positioned in cell body

Figure 4.9 - (Left) front cover A1 (Right) neoprene gasket M

Figure 4.10 - Reference electrode setup, to be connected to luggin capillary H via connection port.

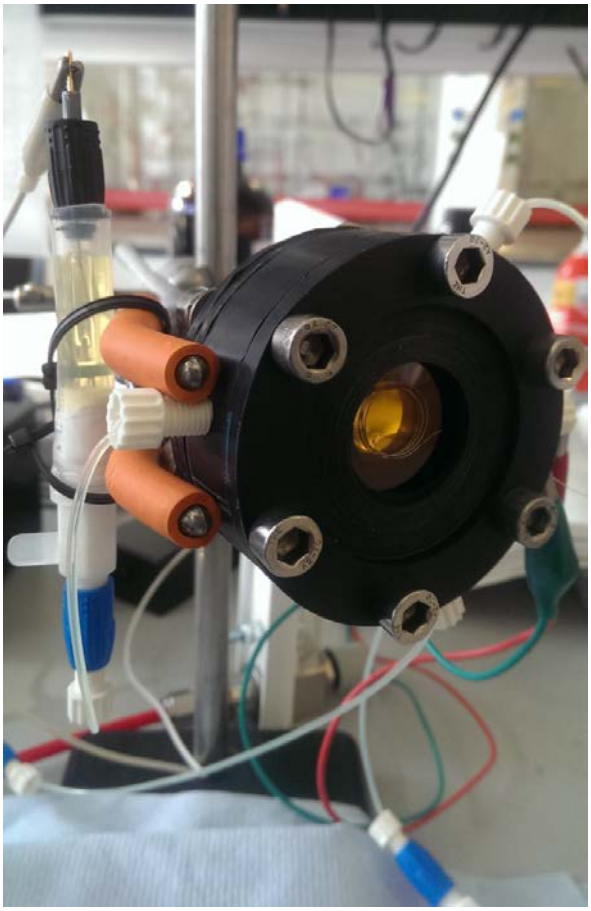

Figure 4.11 - Assembled cell, connected to potentiostat and electrolyte inlet and outlet ports.

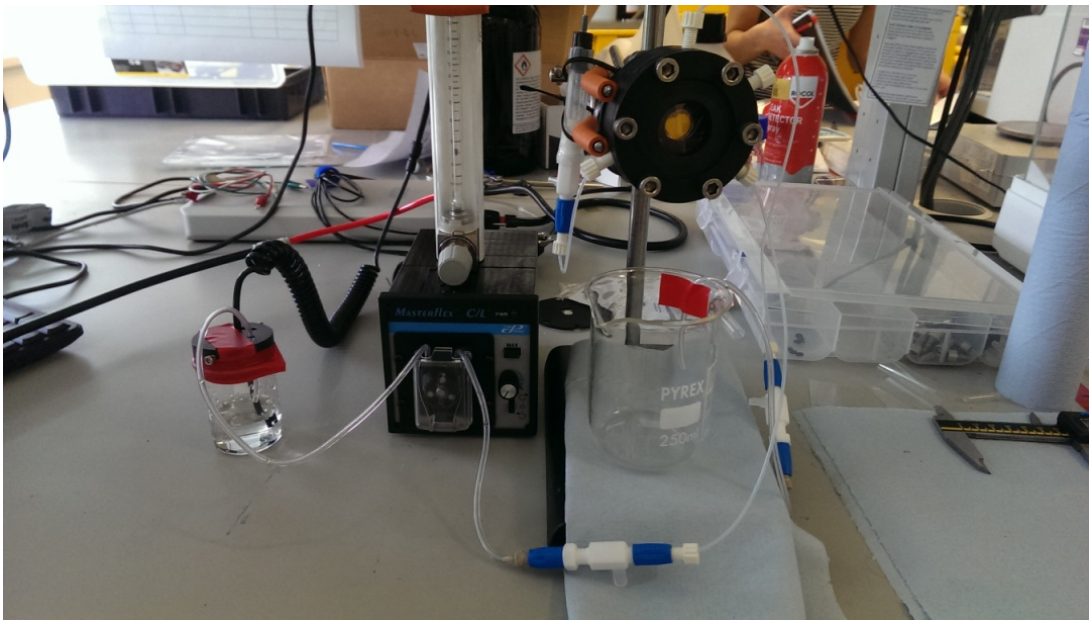

Figure 4.12 - Cell connected to pump supplying electrolyte, electrolyte is purged with nitrogen gas controlled by a flow meter.

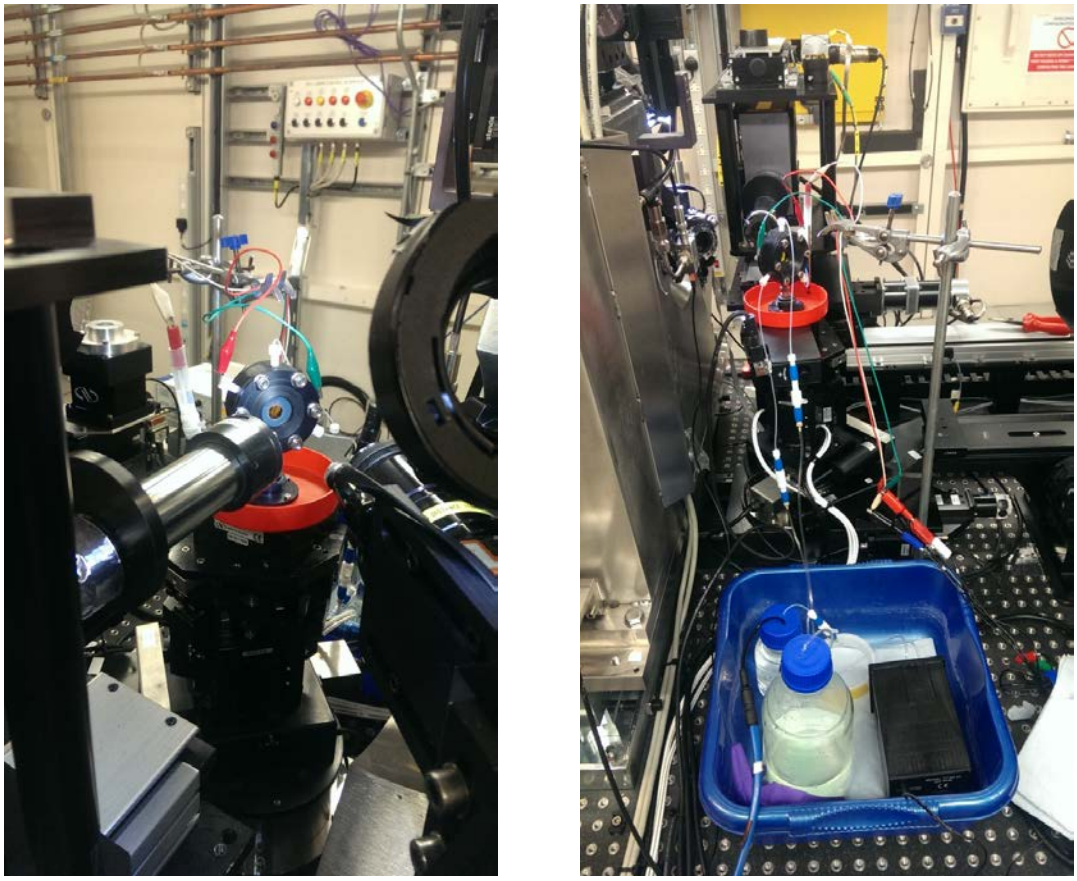

Figure 4.13 - *In situ* cell on I18 beamline, cell fitted onto mounting post with red drip tray, cell connected to pump and nitrogen purged electrolyte and waste bottle, electrodes connected to potentiostat via crocodile clips.

4.3 In situ Cell Development and Challenges

The cell presented in chapter 4 was a result of many lessons learned. The first cell developed seen in figure 4.14, was based around a 1 cm^2 cuvette with 3 electrodes positioned inside; a glass substrate coated with conductive indium tin oxide with a deposited nickel hydroxide thin film, a platinum wire coil to act as a counter electrode and a silver/ silver chloride gel reference electrode.

Figure 4.14 – Initial electrochemical cell setup

Although suitable for *in situ* UV-Vis spectroscopy, this design was not suitable to XRD or EXAFS experiments for several reasons. For EXAFS experiments poor florescence signal from the nickel hydroxide layer would have resulted due to the attenuation from the cuvette, electrolyte, glass substrate and indium tin oxide layer prevented detection of the nickel signal on the beamline for EXAFS experiments. Another issue was the inability to switch electrolyte solutions and easily purge the electrolyte with an inert gas such as nitrogen.

The window material for the final cell design was made from polyethylene terephthalate with an indium tin oxide coating (PET-ITO), to which the nickel hydroxide layer was deposited directly to function as a working electrode. This reduced the attenuation of the X-rays and allowed the cell to work in a fluorescence mode on the I18 beamline and is a novel idea not seen in other cell designs.

The cell develop also had a system of ports and taps which allowed for the filling and drainage of nitrogen purged electrolytes via a peristaltic pump. This reduced the interference of the oxygen evolution reaction during cyclic voltammetry experiments but enabled both thin film deposition with a nickel nitrate solution, washing with deionised water and electrochemical cycling from a potassium hydroxide solution without the need of moving the cell from the beamline, saving time during the beamline experiments.

However, one drawback from the design of a flexible polymer film and a flowing electrolyte system is the pulsing effect from the peristaltic pump causing a small movement of the deposited film, this could be overcome in future work with a pulseless pump design or a less flexible working electrode.

Another issue that was encountered was that intense XRD reflection from the indium tin oxide layers over shadowed the weak peaks of nickel hydroxide layer, although this was not able to be resolved at the time, either an alternative conductive layer could be used or the cell could be used for analysis of another material which XRD peaks do not coincide with indium tin oxide.

Another challenge was that the configuration of the three electrodes was not ideal, leading to a quasi-reversible system as shown in figure 4.15 caused by high ohmic drop. This could be overcome by increasing the concentration of the electrolyte or by reconfiguring the 3 electrodes by reducing the surface area of the working electrode, increasing the surface area of the counter electrode and brining the reference electrode closer to the working electrode.

4.4 Cell performance

The novel electrochemical cell design has a high level of functionality with its ability to perform UV-Vis spectroscopy and XAFS, µXRF and XRD measurements. The design allows for XRD measurements however, this proved challenging as the reflections associated with the nickel hydroxide material were very weak in comparison to those associated with the ITO, which was present as a coating on the polymer as well as the strong attenuation of the X-rays in the electrolyte.

As mentioned previously the ability to flow electrolyte through the cell enables the nickel hydroxide film to be grown from a nickel nitrate solution, washed with deionised water then colour cycled in a potassium hydroxide solution all *in situ* and without the need for disassembly of the system. The ability to flow the liquid through the cell means that the electrolyte can be purged with nitrogen in a separate vessel and pumped through the cell. Care must be taken however to rinse the cell well with deionised water between changing electrolytes as the addition of potassium hydroxide to nickel nitrate solution forms a precipitate of nickel hydroxide on the inside of the cell, window, taps and components. Another issue with using a flexible film as an X-ray window is the pulsing effect from the peristaltic pump, this could be overcome with a different pump design or using different window material.

The cell was assembled using screws with metal thread coils inserted into the main body of the cell. However over time the tightening and un-tightening of the screws caused the nylon threads to strip. This was overcome by using 6 bolts passed through the cell with nuts and washers to compress the cell. A more robust design could be made using a material such as stainless steel which could be internally insulated with PTFE.

Although the working electrode performed well, the connection using the gold wire to the potentiostat proved fragile and was a critical point of weakness for the cell. If the gold wire could be supported in the same way as the platinum wire counter electrode and insulated (as the high conductivity would cause preferential deposition over the ITO polyester film) then this would improve the cells durability.

As shown in figure 4.14 the electrochemical cell showed a quasi-reversible redox behaviour when cyclic voltammetry was performed at scan rates of 1-64 mV s^{-1} of a blank ITO electrode in a nitrogen purged solution of 10 mM potassium ferricyanide in 1 M potassium nitrate solution. The quasi-reversible shape is most likely due to the uneven current distribution due to the large surface area of the working electrode in comparison to the platinum wire counter electrode.

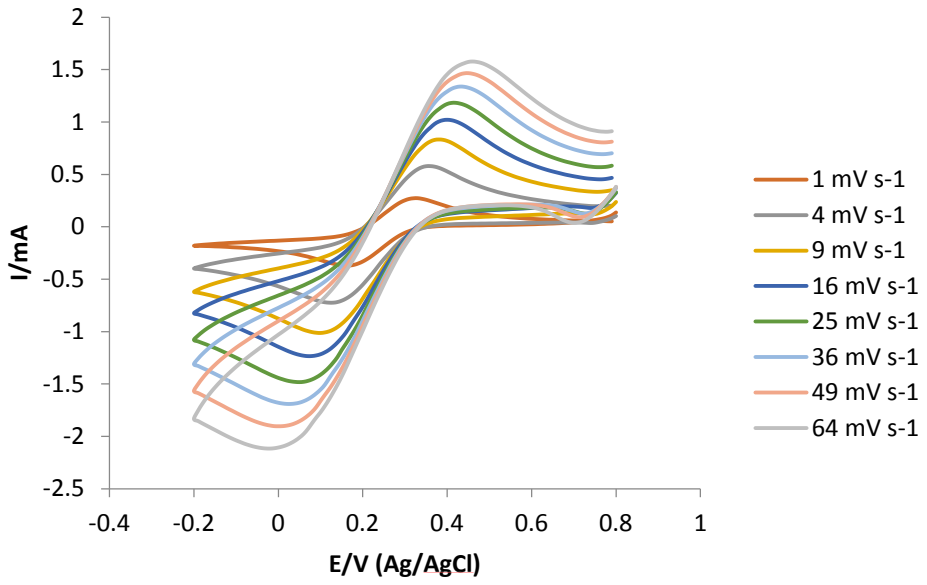

Figure 4.15 – Cyclic voltammogram of the *in situ* cell performing a potassium ferri/ferrocyanide redox couple reaction.

Figure 4.16 shows the electrochromic colour switching behaviour of the cell in a UV-Vis spectrophotometer measuring the Δ_{max} at 550 nm. The reduction in contrast between the bleached and coloured states could be due to the transition of α-

$Ni(OH)_2$ to β-$Ni(OH)_2$. In figure 4.17 the electrochromic colour switching can be seen using a white LED illuminating the film through the cell.

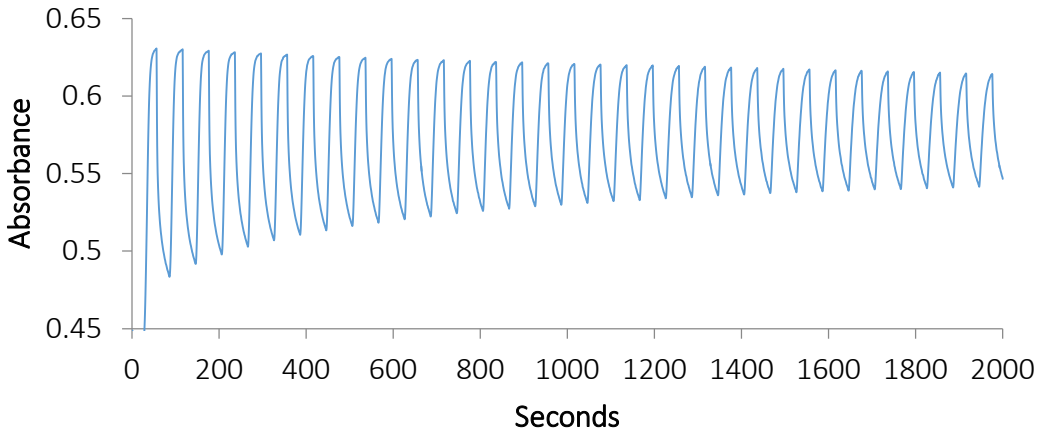

Figure 4.16 – UV-Vis absorbance of cell window during double step chronopotentiometry, absorbance measured at 550 nm, film deposited 200 s, -0.1 mA cm^{-1} in a solution of $Ni(NO_3)_2$ (0.01 M), potential switched from -0.2 V to +0.6 V in 0.1 KOH solution.

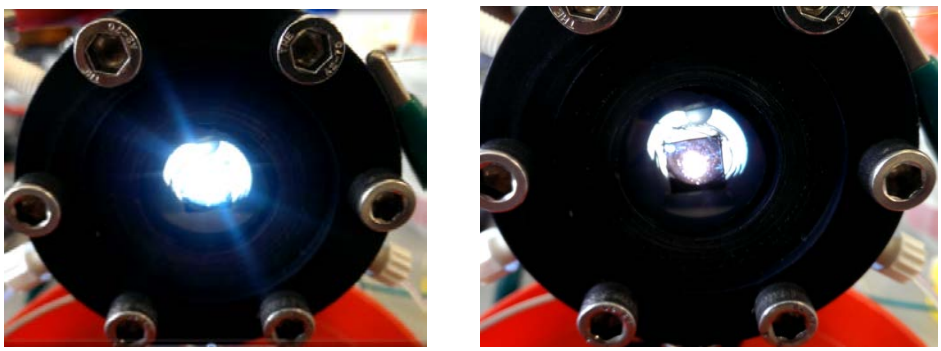

Figure 4.17 – Photographs of the *in situ* cell illuminated from behind by a white LED under potential control (left) applied potential -0.2 V (vs Ag/AgCl) (right) applied potential +0.6 V (vs Ag/AgCl) in 0.1 M KOH

Figure 4.18 below shows the shift of the edge step in the XANES spectrum of the nickel hydroxide film measured in fluorescence mode as the potential is increased from 0.0 V to +0.6 V (vs Ag/AgCl). As the nickel hydroxide film is converted to nickel oxyhydroxide at the more positive potentials and the edge step is shifted to higher energies. This shows that cell can perform the desired function of measuring the nickel hydroxide films *in situ* and further studies can be made.

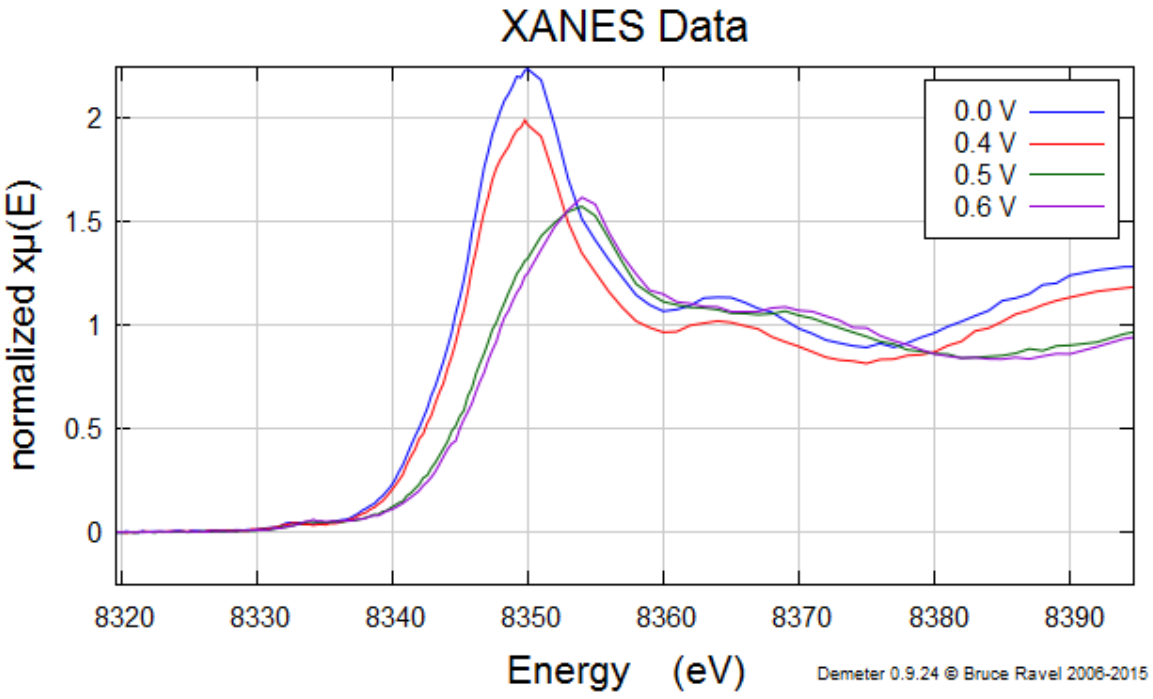

Figure 4.18 - *In situ* XANES data of nickel hydroxide thin film, potential stabilised for 10 minutes before taken XANES measurements 0.0 V, 0.4 V, 0.5 V, 0.6 V (Vs. Ag/AgCl) in 0.1 M KOH.

Chapter 5

Conclusion and Further work

5.1 Conclusion

This thesis shows that different phases of nickel hydroxide can be synthesised through the chemical precipitation methods by changing the experimental parameters of base, temperature and reaction duration. Reaction conditions for α-$Ni(OH)_2$ β-Ni(OH, β_{BC}-$Ni(OH)_2$, β*-$Ni(OH)_2$ have been identified.

An electrochemical cell was developed for the analysis for electrochromic nickel hydroxide thin films for *in situ* XAFS measurements, we have obsereved the X-ray absorption edge shift to higher energies when the nickel hydroxide film is oxidised to nickel oxyhydroxide. The cell has also shown that it can be used to demonstrate the reversible electrochromic switching effect of the nickel hydroxide film using UV-Vis spectroscopy.

Unfortunaly *in situ* XRD data of the thin films was not obtained due to the intense reflections of the ITO coating on the working electrode and the weak and the high level of X-ray attenuation from the potassium hydroxide electrolyte.

5.2 Further work

This work has laid the foundation for future investigations for not only nickel hydroxide research but also *in situ* electrochromic studies. Recommended future work would include; improvements to the current electrochemical design to make it more robust and reliable, studies on the crystallographic phases present of nickel hydroxide thin films and their transition of the α/γ to β/β redox couple, the effect of doping nickel hydroxide films with other metallic element in order to improve the electrochromic performance.

References

1. J. McBreen, in *Handbook of battery materials*, ed. J. O. Benenhard, Wiley-VCH, 1st edn., 1999, pp. 135–151.

2. H. Li, S. Liu, C. Huang, Z. Zhou, Y. Li, and D. Fang, *Electrochim. Acta*, 2011, **58**, 89–94.

3. J. Chen and J. Zheng, *J. Electroanal. Chem.*, 2015, **749**, 83–88.

4. J. P. Cronin, T. J. Gudgel, S. R. Kennedy, A. Agrawal, and D. R. Uhlmann, *Mater. Res.*, 1999, **2**, 1–9.

5. H. Bode, K. Dehmelt, and J. Witte, *Electrochim. Acta*, 1966, **11**, 1079–1087.

6. P. Oliva, J. Leonardi, J. F. Laurent, C. Delmas, J. J. Braconnier, M. Figlarz, F. FIevet, and A. de Guibert, *J. Power Sources*, 1982, **8**, 229–255.

7. D. S. Hall, D. J. Lockwood, C. Bock, and B. R. MacDougall, *Proc. Math. Phys. Eng. Sci.*, 2015, **471**, 20140792.

8. C. G. Granqvist, *Thin Solid Films*, 2014, **564**, 1–38.

9. C. Desmazures, 1889.

10. A. Bernard and R. Lauwerys, *Experientia. Suppl.*, 1986, **40**, 114–23.

11. J. Chen, University of Wollongong, 1999.

12. J. D. Dunlop, G. M. Rao, and T. Y. Yi, *NASA Handbook for Nickel Hydrogen Batteries*, National Aeronautics and Space Administration. Scientific and Technical Information Branch, Scientific and Technical Information Branch, 1993.

13. H. B. Li, M. H. Yu, F. X. Wang, P. Liu, Y. Liang, J. Xiao, C. X. Wang, Y. X.

Tong, and G. W. Yang, *Nat. Commun.*, 2013, **4**, 1894.

14. M. K. Carpenter and D. A. Corrigan, *J. Electrochem. Soc.*, 1989, **136**, 1022.

15. R. L. Doyle, I. J. Godwin, M. P. Brandon, and M. E. G. Lyons, *Phys. Chem. Chem. Phys.*, 2013, **15**, 13737–83.

16. H. Bode, K. Dehmelt, and J. Witte, *Electrochim. Acta*, 1966, **11**, 1079–1087.

17. T. Marcopoulos and M. Econotraou, *Am. Mineral.*, 1981, **66**, 1020–1021.

18. M. Rajamathi, P. V. Kamath, and R. Seshadri, *J. Mat. Chem*, 2000, **10**, 503–506.

19. N. Monenor and G. Dalrio, *Am. Mineral.*, 1973, **58**, 835–839.

20. M. Rajamathi, P. Vishnu Kamath, and R. Seshadri, *J. Mater. Chem.*, 2000, 10, 503–506.

21. O. Glemser and J. Einerhand, *Z. anorg. Chem*, 1950, **261**, 43–51.

22. M. Rajamathi, G. N. Subbanna, P. V. Kamath, N. Subbanna, P. V. Kamath, G. N. Subbanna, and P. V. Kamath, *J. Mater. Chem.*, 1997, **7**, 2293–2296.

23. R. S. Jayashree, P. V. Kamath, and G. N. Subbanna, *J. Electrochem. Soc.*, 2000, **147**, 2029.

24. R. Oesten, M. Wohlfahrt-Mehrens, S. Ströbele, M. Kasper, and R. A. Huggins, *Ionics (Kiel).*, 1996, **2**, 293–301.

25. T. N. Ramesh and P. V. Kamath, *J. Power Sources*, 2006, **156**, 655–661.

26. T. N. Ramesh and P. Vishnu Kamath, *Bull. Mater. Sci.*, 2008, **31**, 169–172.

27. M. K. Carpenter, R. S. Conell, and D. R. Corrigan, *Sol. Energy Mat.*, 1987, **16**,

333–346.

28. Muhammad Z Sialvi, Loughborough University, 2013.

29. A. Delahaye-Vidal, B. Beaudoin, N. Sac-Epée, K. Tekaia-Elhsissen, A. Audemer, and M. Figlarz, *Solid State Ionics*, 1996, **84**, 239–248.

30. D. S. Dalavi, R. S. Devan, R. S. Patil, Y.-R. Ma, and P. S. Patil, *Mater. Lett.*, 2013, **90**, 60–63.

31. R. C. Korošec and P. Bukovec, 2006, 136–147.

32. X. C. Lou, X. J. Zhao, Y. L. Xiong, and X. T. Sui, *J. Sol-Gel Sci. Technol.*, 2010, **54**, 43–48.

33. Q. Song, Z. Tang, H. Guo, and S. L. I. Chan, *J. Power Sources*, 2002, **112**, 428–434.

34. B. Hu, S.-F. Chen, S.-J. Liu, Q.-S. Wu, W.-T. Yao, and S.-H. Yu, *Chemistry*, 2008, **14**, 8928–38.

35. D. S. Hall, C. Bock, and B. R. Macdougall, *J. Electrochem. Soc.*, 2013, **160**, 235–243.

36. G. J. D. A. A. Soler-illia, A. E. Regazzoni, and M. A. Blesa, 1999, 3140–3146.

37. M. Vidotti, R. P. Salvador, E. A. Ponzio, and S. I. Córdoba de Torresi, *J. Nanosci. Nanotechnol.*, 2007, **7**, 3221–3226.

38. L. Demourgues-guerlou and C. Delmas, 1994, **141**, 6–10.

39. M. Morishita, S. Ochiai, T. Kakeya, T. Ozaki, Y. Kawabe, M. Watada, S. Tanase, and T. Sakai, *J. Electrochem. Soc.*, 2008, **155**, A936–A944.

40. P. V. Kamath and G. H. A. Therese, *J. Solid State Chem.*, 1997, **41**, 38–41.

41. M. Oshitani, H. Yufu, K. Takashima, S. Tsuji, and Y. Matsumaru, *J. Electrochem. Soc.*, 1989, **136**, 1590–1593.

42. S. Kim, D. A. Tryk, M. R. Antonio, R. Carr, and D. Scherson, *J. Phys. Chem*, 1994, **98**, 10269–10276.

43. D. A. Corrigan, T. W. Capehart, K. I. Pandya, and R. W. Hoffman, *Nickel Hydroxide Electrodes*, The electrochemical Society, 1990.

44. K. Provazi, M. J. Giz, L. H. Dall'Antonia, and S. I. Córdoba de Torresi, *J. Power Sources*, 2001, **102**, 224–232.

45. V. Pralong, a. Delahaye-Vidal, B. Beaudoin, J.-B. Leriche, and J.-M. Tarascon, *J. Electrochem. Soc.*, 2000, **147**, 1306.

46. R. S. Jayashree and P. V. Kamath, *J. Electrochem. Soc.*, 2002, **149**, A761.

47. H. Wang, Y. Liang, M. Gong, Y. Li, W. Chang, T. Mefford, J. Zhou, J. Wang, T. Regier, F. Wei, and H. Dai, *Nat. Commun.*, 2012, **3**, 917.

48. D. A. Corrigan, *Sol. Energy Mater. Sol. Cells*, 1992, **25**, 293–300.

49. D. A. Corrigan and R. M. Bendert, *J. Electrochem. Soc*, 1989, **136**, 723–728.

50. K. Watanabe, T. Kikuoka, and N. Kumagai, *J. Appl. Electrochem.*, 1995, **25**, 219–226.

51. C. Tessier, C. Faure, L. Guerlou-Demourgues, C. Denage, G. Nabias, and C. Delmas, *J. Electrochem. Soc.*, 2002, **149**, A1136.

52. L. Guerlou-Demourgues, C. Denage, and C. Delmas, *J. Power Sources*, 1994, **52**, 269–274.

53. L. Guerlou-Demourgues and C. Delmas, *J. Power Sources*, 1994, **52**, 275–

281.

54. C. Tessier, P. H. Haumesser, P. Bernard, and C. Delmas, *J. Electrochem. Soc.*, 1999, **146**, 2059–2067.

55. L. Demourgues-Guerlou, J. J. Braconnier, and C. Delmas, *J. Solid State Chem.*, 1993, 104, 359–367.

56. L. Demourgues-Guerlou and C. Delmas, *J. Power Sources*, 1993, **45**, 281–289.

57. L. Trotochaud, S. L. Young, J. K. Ranney, and S. W. Boettcher, *J. Am. Chem. Soc.*, 2014, **136**, 6744–53.

58. D. A. Corrigan, 1980, **134**, 377–384.

59. M. Balasubramanian, C. A. Melendres, and S. Mini, *J. Phys*, 2000, **104**, 4300–4306.

60. M. Morishita, T. Kakeya, S. Ochiai, T. Ozaki, Y. Kawabe, M. Watada, and T. Sakai, *J. Power Sources*, 2009, **193**, 871–877.

61. P. M. S. Monk, R. J. Mortimer, and D. R. Rosseinsky, *Electrochromism and Electrochromic Devices*, Cambridge Univsersity Press, 2007.

62. Southampton Electrochemistry Group., *Instrumental methods in electrochemistry*, 2003.

63. N. Farley, S. Gurman, and A. Hillman, *Electrochem. commun.*, 1999, **1**, 449–452.

64. I. J. Shannon, T. Maschmeyer, G. Sankar, J. Meurig, R. D. Oldroyd, M. Sheehy, D. Madill, A. M. Waller, and R. P. Townsend, *Catal. Letters*, 1997, **44**,

23–27.

65. C. A. Melendres and A. N. Mansour, 1998, **43**, 631–634.

66. G. Xuan, S. Jang, G. Kwag, and S. Kim, *Notes*, 2005, **26**, 671–674.

67. J. Desilvestro, D. A. Corrigan, and M. J. Weaver, *J. Electrochem. Soc*, 1988, **135**, 885–892.

68. Http://www.diamond.ac.uk/Science/Machine/Components.html, 2017.

69. G. Bunker, *Introduction to XAFS*, Cambridge Univsersity Press, 2010.

70. M. Newville, *Rev. Mineral. Geochemistry*, 2014, **78**, 33–74.